



## Sharp interface simulations with Local Mesh Refinement for multi-material dynamics in strongly shocked flows

Shiv Kumar Sambasivan<sup>1</sup>, H.S. UdayKumar\*

*Department of Mechanical and Industrial Engineering, 3131 Seamans Center, University of Iowa, Iowa City, IA 52242, USA*

### ARTICLE INFO

#### Article history:

Received 20 April 2010

Accepted 22 April 2010

Available online 29 April 2010

#### Keywords:

Sharp Interface Methods

Cartesian grid methods

Adaptive Mesh Refinement

Local Mesh Refinement

Ghost Fluid Method (GFM)

Compressible multiphase flows

Compressible multi-material flows

Shock-interface interactions

### ABSTRACT

Shock waves interacting with multi-material interfaces in compressible flows result in complex shock diffraction patterns involving total or partial reflection, refraction and transmission of the impinging shock wave. To simulate such complicated interfacial dynamics problems, a fixed Cartesian grid approach in conjunction with levelset interface tracking is attractive. In this regard, a unified Riemann solver based Ghost Fluid Method (GFM) is developed to accurately resolve and represent the embedded solid and fluid object(s) in high speed compressible multiphase flows. In addition, the Riemann solver based GFM approach is augmented with a quadtree (octree in three-dimensions) based Local Mesh Refinement (LMR) technique for efficient and high fidelity computations involving strong shock interactions. The paper reports on a conservative formulation for accurate calculation of ENO-based numerical fluxes at the fine-coarse mesh boundaries. The numerical examples presented in this paper clearly demonstrate that the methodology produces accurate benchmark solutions and effectively captures fine structures in the flow field.

© 2010 Elsevier Ltd. All rights reserved.

### 1. Introduction

Cartesian grid approaches have become immensely popular because such methods do not suffer from the complex grid generation and grid management requirements inherent to moving mesh and Arbitrary Lagrangian Eulerian (ALE) [6] methods. For moving boundary problems, particularly where interfaces are tracked and treated as sharp entities, Cartesian grid methods retain the simplicity associated with discretization of governing equations while shifting the onus to the numerical treatment at the embedded interface. While the Cartesian grid approach significantly alleviates the complexity associated with mesh management, the method lacks flexibility in effective and automatic grid point placement in regions with rich structures in the flow field. To address this shortcoming, Cartesian grid adaptation has been developed since the pioneering work by Berger and co-workers [7,8]. There are several approaches that have been used to accomplish grid adaptation both in compressible [7,51,30,47,4,74] and incompressible flows [67,28,43,72,42]. Among the aforementioned mesh enrichment techniques, the Adaptive Mesh Refinement (AMR) scheme has found extensive application. AMR generates blocks of structured, non-overlapping, Cartesian mesh patches over

the underlying coarse mesh, and the flow field is evolved on all mesh patches. However, in the context of sharp interface multi-material simulations, Nourgaliev et al. [47] have identified potential pitfalls of the AMR approach for interfaces separating fluids of high impedance mismatch. The AMR approach described in [47] uses a non-conservative natural neighbor interpolation (NNI) [9,65] method that carefully avoids interpolation across the interface of the embedded object, but results in complications in the implementation that detract from the inherent simplicity of the AMR scheme. Alternatively, one could use a generic grid adaptation technique such as the hierarchical tree-based Local Mesh Refinement (LMR) [72] scheme, that does not require repeated interpolation and evolution of the flow field on all grid levels. This latter approach is the one elaborated in the present work. In essence, the following efforts are reported in this paper:

1. A robust, Riemann solver-based GFM approach to resolve shock-interface interactions in high speed compressible multiphase flows is presented. For embedded fluid objects, a Riemann problem is constructed normal to the interface and the solution obtained from solving this Riemann problem is used to populate the ghost cells [55]. For embedded solid objects, a reflective boundary condition is used in conjunction with a Riemann solver to populate the ghost points [54].
2. A simple, conservative formulation (due to Berger et al. [7]) for accurate computation of ENO-based numerical fluxes at the fine-coarse mesh boundaries in tree-based LMR schemes is developed. Since higher-order treatment for temporal evolution

\* Corresponding author. Tel.: +1 319 3355668; fax: +1 319 3355669.

E-mail addresses: [shiv@lanl.gov](mailto:shiv@lanl.gov) (S.K. Sambasivan), [ush@engineering.uiowa.edu](mailto:ush@engineering.uiowa.edu) (H.S. UdayKumar).

<sup>1</sup> Present address: Theoretical Division, Group T-5, MS-B284, Los Alamos National Laboratory, Los Alamos, NM 87545, USA. Tel.: +1 505 665 8075.

(a third order TVD-based Runge–Kutta scheme [59]) and spatial discretization (third order convex ENO scheme [41]) of the governing equations are employed, the evaluation of numerical fluxes at fine-coarse mesh interfaces is not trivial. In particular, higher-order schemes such as ENO/WENO use wider support cells that demand a conservative approach to compute numerical fluxes at mesh interfaces. Application of third and higher-order ENO/WENO schemes have been proven computationally effective only for uniform and smoothly varying curvilinear meshes [58]. Limited progress has been made in this direction to couple higher-order schemes with tree-based grid adaptive schemes. Recently, Cecil et al. [13] have developed a generalized ENO schemes on octree-based unstructured non-uniform meshes. However, the applications reported in their work are limited to one-dimensional weak shocks traversing in single fluid medium. The current work focuses on extending such an approach for strong shock applications and to shock-interface interactions. In addition to the conservative flux computation at the fine-coarse mesh interface, a simple criterion for identifying and tagging cells for refinement is also presented. In direct contrast to the coupling algorithm reported in [47], the present approach retains the simplicity associated with the GFM-based interface capturing technique and the ENO flux construction procedure.

3. High-fidelity computations of shock waves interacting with stationary and moving object(s) are presented. While the previous research efforts reported in [47,74,7,51] were primarily concerned with the resolution of either embedded solid or fluid objects, here shocks interacting with both fluid and solid objects have been computed. The broad range of results presented in this work demonstrate the flexibility and robustness of the current method in efficiently resolving dominant features and disparate length scales for a wide spectrum of Mach numbers.

## 2. Governing equations

The governing equations comprise of hyperbolic conservation laws, cast in Cartesian coordinates:

$$\frac{\partial \vec{U}}{\partial t} + \frac{\partial \vec{F}}{\partial x} + \frac{\partial \vec{G}}{\partial y} = \Phi_A \vec{S}, \quad (1)$$

where

$$\begin{aligned} \vec{U} &= \begin{pmatrix} \rho \\ \rho u \\ \rho v \\ \rho E \end{pmatrix}, \quad \vec{F} = \begin{pmatrix} \rho u \\ \rho u^2 + p \\ \rho uv \\ u(\rho E + p) \end{pmatrix}, \quad \vec{G} = \begin{pmatrix} \rho v \\ \rho uv \\ \rho v^2 + p \\ v(\rho E + p) \end{pmatrix}, \\ \vec{S} &= -\frac{1}{x} \begin{pmatrix} \rho u \\ \rho u^2 \\ \rho uv \\ u(\rho E + p) \end{pmatrix}. \end{aligned} \quad (2)$$

Here  $E = e + \frac{1}{2}(u^2 + v^2)$  is the total specific internal energy and  $e$  is specific internal energy. The switch function  $\Phi_A$  is set to zero for two-dimensional problems. In the case of axisymmetric problems with  $y$ -axis being the axis of symmetry, the switch function  $\Phi_A$  is set to 1. Closure for the above set of governing equations is obtained by using a stiffened equation of state [45,29],

$$P = \rho e(\gamma - 1) - \gamma P_\infty, \quad (3)$$

where  $\gamma$  is the specific heat ratio (the Grüneisen exponent [45,71] for stiff fluids) and  $P_\infty$  is a material dependent constant [17]. For the case of ideal gas we have  $\gamma = \frac{c_p}{c_v}$  and  $P_\infty = 0$ . For stiff fluids like water,  $\gamma$  and  $P_\infty$  take the values of 5.5 and 0.613 GPA respectively. From the definition of sound speed, we have

$$c^2 = \left( \frac{\partial P}{\partial \rho} \right)_{s=\text{constant}}. \quad (4)$$

Using Eq. (3), the speed of sound becomes

$$c = \sqrt{\frac{\gamma(P + P_\infty)}{\rho}}. \quad (5)$$

## 3. Sharp interface treatment via Ghost Fluid Method (GFM)

As in previous work [55,54], levelsets [48] are used to represent and track the embedded interface. The tracked interface has to be coupled with the flow solver such that the jump in the mass, momentum and energy fluxes, along with the material properties across the interface, are represented accurately. In the GFM approach [23], this translates to suitably populating the ghost points with ghost fields that depict the interface type and conditions accurately. The definition of the ghost states in turn depends on the material enclosed by the embedded object(s). In this section, the GFM-based interface treatment techniques developed for resolving embedded fluid [55] and solid [54] objects are briefly reviewed. For additional details, the reader may refer to the original articles [55,54] and the references cited therein.

### 3.1. Fluid fluid interface treatment technique

For embedded fluid objects such as droplets or bubbles interacting with strongly shocked flows, it has been well established that the original approach of entropy extrapolation (*isobaric fix* due to Fedkiw et al. [23]) for the definition of ghost states fails to maintain a non-oscillatory pressure field, particularly when strong shock and detonation waves reside in close proximity to the interface [40]. In such situations, in order to capture the interface conditions precisely it is required to accurately resolve the wave interactions occurring at the interface [40]. Therefore, a Riemann problem is constructed normal to the interface and the solutions obtained from solving the Riemann problem are employed to define the ghost states. In [55], a simple and a robust method is developed to incorporate the Riemann problem at the interface. The methodology developed takes into account the subcell position and the topology of the interface in the (Riemann problem) construction procedure. The Riemann problem is solved exactly, and the solutions obtained are enforced to determine the flow properties at the ghost points. It has been shown in [55] that the method is stable and accurate for a wide range of shock strengths, and also for interfaces separating materials of high impedance mismatch. In what follows, the Riemann problem construction procedure is briefly reviewed.

#### 3.1.1. Procedure to construct the riemann problem at the interface

In order to construct the Riemann problem at the interface, a probe is inserted from each interfacial point (interfacial points are grid points that straddle the zero level set field) such as point  $P$  in Fig. 1. The coordinates of the point of intersection of the probe and the interface, i.e. point IP in Fig. 1, can be determined using the value of the level set field at point  $P$ :

$$\vec{X}_{\text{IP}} = \vec{X}_P + |\phi_P| \vec{N}_P. \quad (6)$$

The left and the right states required for assembling the Riemann problem are obtained by advancing a distance of  $1.5 \Delta x$  into the real fluids, on either side of the interface. The length of the probe ( $1.5 \Delta x$ ) is critical, and is chosen such that the interfacial point  $P$ , for which the Riemann problem is being constructed, bears no or minimal weight in the interpolation procedure involved in defining the Riemann problem. This enables the Riemann problem to be

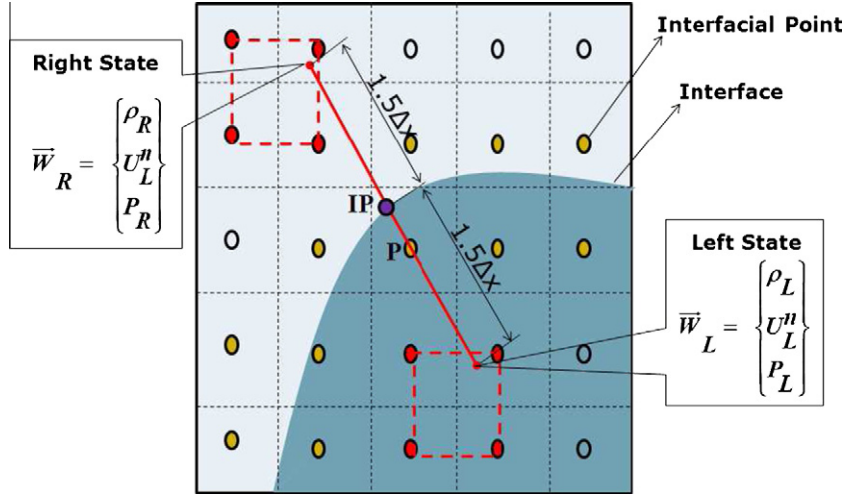


**Fig. 1.** Procedure to construct the Riemann Problem at the interface.

constructed with points which are not infused with the errors generated at the interface [17]. In order to maintain consistency, the point which lies inside the level set is always denoted as the left state and the point which lies outside the level set is always denoted as the right state. Thus the coordinates of the points corresponding to the left and right states can be computed as follows:

$$\vec{X}_L = \vec{X}_{IP} - 1.5\Delta x \vec{N}_P, \quad (7)$$

$$\vec{X}_R = \vec{X}_{IP} + 1.5\Delta x \vec{N}_P. \quad (8)$$

The flow properties ( $\vec{W}_{LR}$ ) corresponding to the left ( $\vec{X}_L$ ) and the right ( $\vec{X}_R$ ) states can then be obtained using a simple bilinear interpolation procedure as shown in Fig. 1. Once the left and the right states are determined, the resulting Riemann problem can be solved using standard Riemann solver techniques [70]. The solutions obtained from solving the Riemann problem are then extended to define the ghost points.

### 3.2. Solid-fluid interface treatment

There are significant differences between the treatment of fluid-fluid and solid-fluid interfaces in the ghost fluid framework. In the case of fluid-fluid interfaces, the flow variables such as velocity and pressure, are available (on both sides of the interface) to construct the Riemann problem at the interface. For solid-fluid interfaces, due to the absence of flow fields in the solid side, it is not immediately clear how to populate the ghost points with the appropriate extended flow properties. However, at the interface of a solid body immersed in compressible flows, the following boundary conditions apply for velocity, temperature and pressure fields:

$$v_n = U_n, \quad (9)$$

$$\frac{\partial v_{t_1}}{\partial n} = 0, \quad (10)$$

$$\frac{\partial v_{t_2}}{\partial n} = 0, \quad (11)$$

$$\frac{\partial T}{\partial n} = 0, \quad (12)$$

$$\frac{\partial p}{\partial n} = \frac{\rho v_{t_1}^2}{R} - \rho a_n. \quad (13)$$

The above set of boundary conditions govern the behavior of the inviscid fluid near the embedded solid body and must be enforced on the real fluid by suitably populating the ghost points. In [54], a reflective boundary condition (RBC) approach was employed to

accurately enforce the aforementioned boundary conditions at the interface.

In a manner similar to the Riemann problem construction procedure, a probe is inserted from each *interfacial ghost point* (in the solid phase) to determine the corresponding reflected point in the fluid phase. For instance, the reflected point IP1 (Fig. 2) on the real fluid side corresponding to ghost point P can be obtained as follows:

$$\vec{X}_{IP1} = \vec{X}_P + 2|\phi_P| \vec{N}_P. \quad (14)$$

The flow conditions at the reflected point IP1 can be determined by employing a bilinear interpolation procedure as follows.

For any reflected point, such as point IP1 in Fig. 2, the surrounding interpolating points 1, 2, 3 and IP are identified. At point IP on the interface, the value of the flow variables (Dirichlet conditions) or the flow gradient (Neumann type conditions) is available. Thus to complete the interpolation procedure, the appropriate boundary conditions (Eq. 9) are embedded in a bilinear interpolant. The value of the flow variables at the reflected point IP1 can be obtained using bilinear interpolation:

$$\psi = a_1 + a_2 x_{IP1} + a_3 y_{IP1} + a_4 x_{IP1} y_{IP1} \quad (15)$$

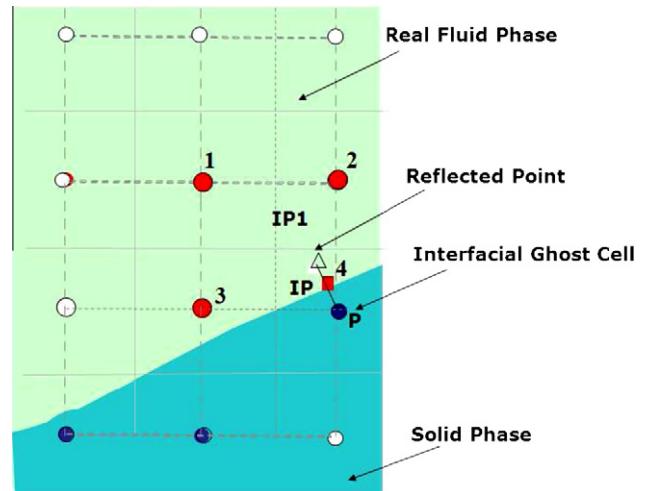


**Fig. 2.** Embedding the boundary conditions with the interpolation procedure for resolving immersed solid objects.

where  $(x_{IP1}, y_{IP1})$  are the coordinates of the reflected point IP1 and  $\psi$  corresponds to the flow variables. In order to determine the coefficients  $a_1 \rightarrow a_4$ , Eq. (15) is applied to the surrounding points chosen for the interpolation procedure. Hence, for Dirichlet type boundary conditions Eq. (15) reduces to,

$$\begin{pmatrix} 1 & x_1 & y_1 & x_1y_1 \\ 1 & x_2 & y_2 & x_2y_2 \\ 1 & x_3 & y_3 & x_3y_3 \\ 1 & x_{IP} & y_{IP} & x_{IP}y_{IP} \end{pmatrix} \begin{pmatrix} a_1 \\ a_2 \\ a_3 \\ a_4 \end{pmatrix} = \begin{pmatrix} \psi_1 \\ \psi_2 \\ \psi_3 \\ \psi_4 \end{pmatrix} \quad (16)$$

and for Neumann type conditions, we have

$$\begin{pmatrix} 1 & x_1 & y_1 & x_1y_1 \\ 1 & x_2 & y_2 & x_2y_2 \\ 1 & x_3 & y_3 & x_3y_3 \\ 0 & n_x & n_y & n_x y_{IP} + n_y x_{IP} \end{pmatrix} \begin{pmatrix} a_1 \\ a_2 \\ a_3 \\ a_4 \end{pmatrix} = \begin{pmatrix} \psi_1 \\ \psi_2 \\ \psi_3 \\ S_4 \end{pmatrix}. \quad (17)$$

The last row of the coefficient matrix in Eq. (17) is obtained by differentiating Eq. (15), noting that

$$\frac{\partial \psi}{\partial n} = \frac{\partial \psi}{\partial x} n_x + \frac{\partial \psi}{\partial y} n_y, \quad (18)$$

where  $n_x$  and  $n_y$  are the components of the normal vector at point  $P$  and  $S_4$  corresponds to the value of the normal gradient at the interface. After determining the coefficients, the flow properties at the reflected point can be determined using Eq. (15). The ghost points are then populated with flow conditions using the reflected field.

#### 4. Local Mesh Refinement (LMR)

Octree-based mesh refinement schemes are general but come with complexities associated with the data structure, and pose significant challenges for algorithmic implementation [43,42]. The implementational intricacies associated with octree and quadtree-based LMR schemes have been presented by Greaves et al. [24–27]. Although LMR-based adaptive schemes have found limited applications for compressible flow computations [19,18,13,20], one may find a multitude of applications pertaining to incompressible flow simulations [2,75,61,63,62,46,64,49,43,42,38]. Particularly for compressible flow simulations, AMR schemes have been preferred over LMR approach despite of the potential savings in computational resources. Although the reason for this trend is not apparent, it was pointed out in [43,42] that spurious and artificial reflected waves were generated with the use of LMR schemes, when waves of large magnitude were allowed to pass through the fine-coarse mesh boundaries [16]. One possible reason for the generation of such spurious waves is that the low frequency errors on a given fine grid become high frequency errors when passed on to coarse grids [10,77]. As will be evident from the current work, LMR schemes can be employed effectively by judiciously enforcing refinement criteria that prohibit waves from passing the fine-coarse mesh boundaries. The impact of the wave passage through the fine-coarse mesh interfaces has been carefully examined; further discussion on this topic is deferred to Section 5.1.1.

##### 4.1. Coarsening and refinement operations

Cells are refined and coarsened based on the presence of structures and dominant features in the flow field. As the refinement process is solution-adaptive, a base mesh that is fine enough to capture the global flow structure is selected, and the initial levelset field is constructed on this base mesh. Once the base mesh is defined, all those cells that exceed a preset threshold limit of the refinement criteria are tagged, and the refinement operation is car-

ried out on these cells until the desired level of refinement is achieved. The computational cells straddling the interface of the embedded objects, that lie within the narrow band of the levelset field are refined to the maximum level. This eliminates interpolation errors and associated instabilities from being introduced at the interface [60]. Thus initial discontinuities (such as shock and detonation waves) and the cells in the narrow band of the levelset field are uniformly refined to the finest level, and are maintained at the finest level throughout the computation. Other flow structures that develop with evolution of the flow field are refined by repeated application of the refinement criteria at regular intervals in time (determined by the fastest traveling (characteristic) wave in the domain (CFL condition)). In addition, adequate number of buffer cells are provided in refinement zones around strong shock and rarefaction waves. As a band of fine (buffer) cells always surround these flow structures, any new structure formed with the evolution of the flow field will remain within these band of fine cells. This further ensures that interpolations are not performed near discontinuities in the flow field.

Since each time a cell is divided four (eight in three-dimensions) new child cells are formed, a constant refinement factor of 2 is maintained i.e. a cell which is recursively refined  $k$  times (for  $k > 1$ ) forms  $2^k$  child cells. Therefore, a (child) cell at  $k$ th level formed by  $k - 1$  recursive divisions of a parent cell will have sides of length  $\Delta x = \frac{1}{2^{k-1}} \Delta x_g$ , where  $\Delta x_g$  is the size of the base mesh with level 1 denoting the global base mesh.

Divided cells that are not tagged for refinement are coarsened. Whenever a cell is coarsened, the flow properties for the parent cell are determined from aggregating the flow properties from its child cells.

$$\vec{U} = \frac{1}{N_{child}} \sum_{ich=1}^{N_{child}} \vec{U}_{ich}, \quad (19)$$

where  $\vec{U}$  corresponds to the primitive variables and  $N_{child} = 4$  for quadtree and  $N_{child} = 8$  for octree data structures. The flow attributes for the newly formed child cells are derived from interpolating on the leafcells in the preceding time step. One of the most commonly used approach for child cell interpolation in both LMR and AMR framework is the MUSCL-based interpolation scheme [50,51]. Cecil et al. [13] have used higher-order ENO-based interpolations for defining the flow attributes for the newly created child cells. The ENO-based interpolations for child cells were carried out by choosing stencils along the diagonal and grid directions. In this work, a simple conservative bilinear interpolation due to Berger et al. [7] is used to define the flow attributes for the newly created child cells. Noting that the child cells are created and destroyed only at the edges of the buffer cells that surrounds the fine mesh cells encompassing dominant flow features, a simple bilinear interpolation scheme is found to be adequate.

##### 4.2. Refinement criteria

As mentioned before, the refinement criteria identify and tag cells in regions with distinct structures and steep gradients in the flow field. Obtaining a suitable criterion that simultaneously track strong and weak shocks, rarefaction waves, slip-lines and contact discontinuities (material interfaces) is a tricky proposition. The refinement criterion is critical for tree-based mesh adaptive schemes particularly when applied to compressible flow calculations, as interpolations between grid levels near discontinuities are to be avoided. Such interpolations can be averted if the fine-coarse mesh interface is sufficiently far away from discontinuities and the flow field varies smoothly across the mesh interface. Berger et al. [8,7] employed a Richardson extrapolation based estimate of the local truncation error of the solution to identify regions

with discontinuities. A similar approach was used in [37] for astrophysical flow computations. In [77,19,75] a statistical description based on the cell-size-weighted curl and divergence of the velocity field were employed to identify regions that are excessively compressed and sheared. Flow field gradient-based (density, velocity and speed of sound) estimates were used in [78] for refining and coarsening grid patches. Recently, Karni et al. [36] developed a smoothness indicator (SI) based on weak local truncation error estimate to identify roughness and discontinuities in the solution.

The approach appears promising, but may not be computationally efficient as wider support stencil and time history (up to three consecutive time levels) are required to compute the SI. In this work, a simple approach that uses fewer stencils and time history is adopted to identify and tag cells for refinement. The following steps are performed to identify potential cells for refinement:

- At each cell center, 2nd order one sided and 2nd order central difference based derivatives are evaluated as follows:

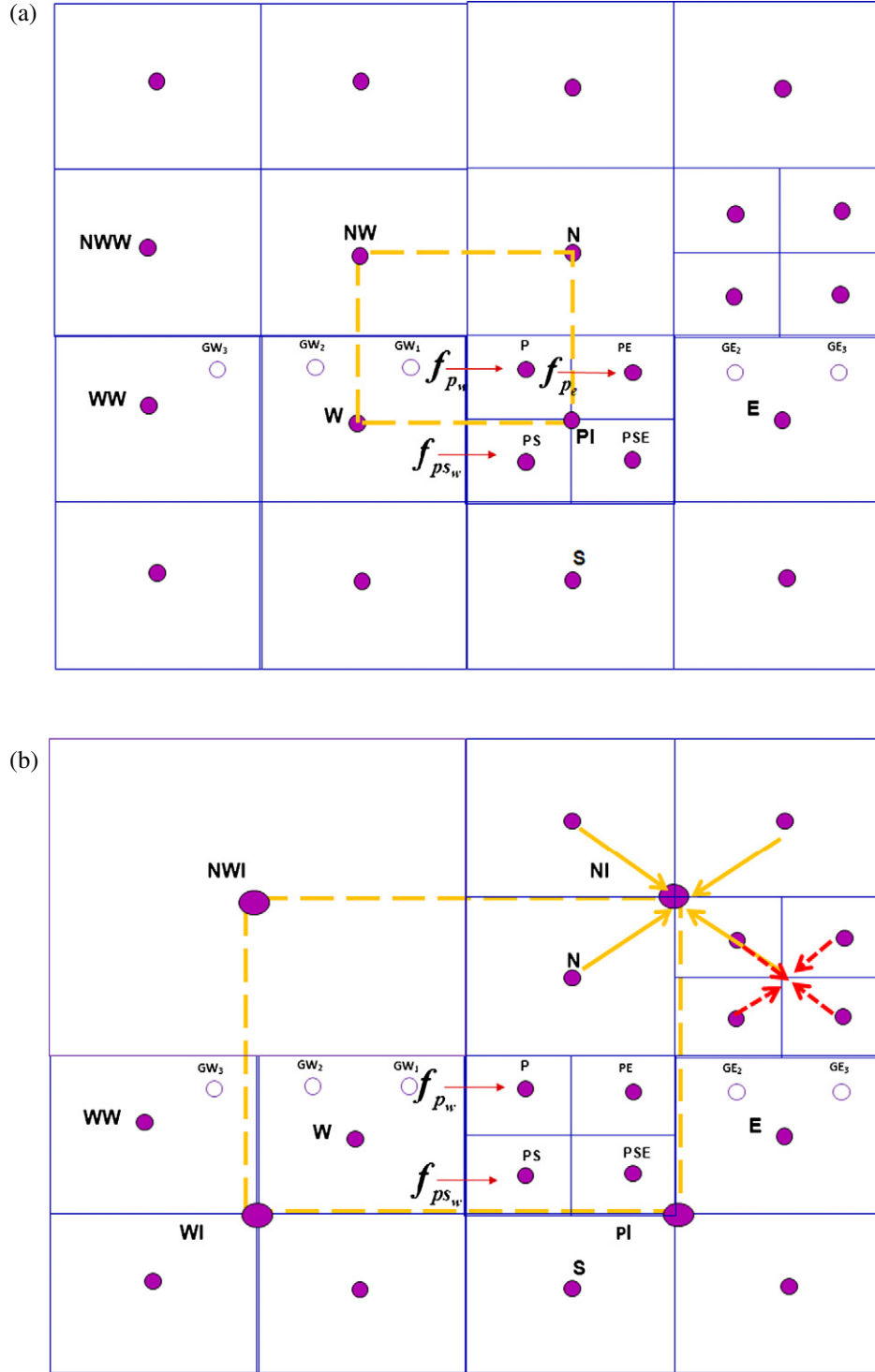


**Fig. 3.** ENO-based flux construction at the fine-coarse mesh boundary with (a) adjoining cells having one level difference (b) adjoining cells having more than one level difference along the diagonal direction.

$$\frac{df(x)^-}{dx} \Big|_{x_i} = \frac{f(x_{i-2}) - 4f(x_{i-1}) + 3f(x_i)}{2\Delta x} + \frac{1}{3} \Delta x^2 \frac{d^3 f(x)}{dx^3}; \\ \forall x \leq x_i, \quad (20)$$

$$\frac{df(x)^+}{dx} \Big|_{x_i} = \frac{-3f(x_i) + 4f(x_{i+1}) - f(x_{i+2})}{2\Delta x} + \frac{1}{3} \Delta x^2 \frac{d^3 f(x)}{dx^3}; \\ \forall x \geq x_i, \quad (21)$$

$$\frac{df(x)}{dx} \Big|_{x_i} = \frac{f(x_{i+1}) - f(x_{i-1})}{2\Delta x} - \frac{1}{6} \Delta x^2 \frac{d^3 f(x)}{dx^3}. \quad (22)$$

- Since in smooth regions, the one-sided estimates approach the central difference value, the one-sided derivatives are compared with the central difference estimate to obtain

$$\xi_1 = \left| \frac{df(x)}{dx} \Big|_{x_i} - \frac{df(x)^-}{dx} \Big|_{x_i} \right|, \quad (23)$$

$$\xi_2 = \left| \frac{df(x)}{dx} \Big|_{x_i} - \frac{df(x)^+}{dx} \Big|_{x_i} \right|, \quad (24)$$

$$\xi_3 = \text{MAX} \left( \left| \frac{df(x)^-}{dx} \Big|_{x_i} \right|, \left| \frac{df(x)}{dx} \Big|_{x_i} \right|, \left| \frac{df(x)^+}{dx} \Big|_{x_i} \right| \right) \quad (25)$$

where  $\xi_1, \xi_2$  and  $\xi_3$  are the estimates of error.

- As the derivatives  $\frac{df(x)^-}{dx} \Big|_{x_i}$ ,  $\frac{df(x)}{dx} \Big|_{x_i}$  and  $\frac{df(x)^+}{dx} \Big|_{x_i}$  are comparable in smooth regions, the error estimates  $\xi_1$  and  $\xi_2$  are of  $O(\Delta x^2)$ . For regions with discontinuities, the error estimates  $\max(\xi_1, \xi_2) \geq \delta_1$  or  $\xi_3 \geq \delta_2$ , where  $\delta_1 > 0$  and  $\delta_2 > 0$  are user-defined tolerance limits. The criterion  $\delta_1$  is primarily used to identify dominant flow structures such as shocks and contact discontinuities, while  $\delta_2$  is used for resolving weak shocks and other weak structures such as expansion waves and slip-lines. Since shocks and contact discontinuities are  $O(1)$  discontinuities, the threshold for the criterion  $\delta_1 \approx O(\Delta x)$ . As will be shown in the results section, based on the numerical experiments conducted in this work,  $\delta_1$  is set in the range  $\delta_1 \Delta x_g \approx \{\Delta x_g - 1.0\}$ , where  $\Delta x_g$  is the size of the base mesh. The value of  $\delta_2$  depends on the features and gradients that the user desires to resolve and suitable choices are indicated in Section 5.2.2. The function  $f$  chosen in the current work correspond to the density, pressure and entropy fields that reside at the centers of the computational cells.

The above procedure is repeated along all grid directions. Since the refinement criterion for a point  $x_i$  uses points  $\{x_{i-2}, x_{i-1}, x_i, x_{i+1}, x_{i+2}\}$  in the neighborhood of  $x_i$ , the procedure is effective in flagging cells that fall in the vicinity of the discontinuity.

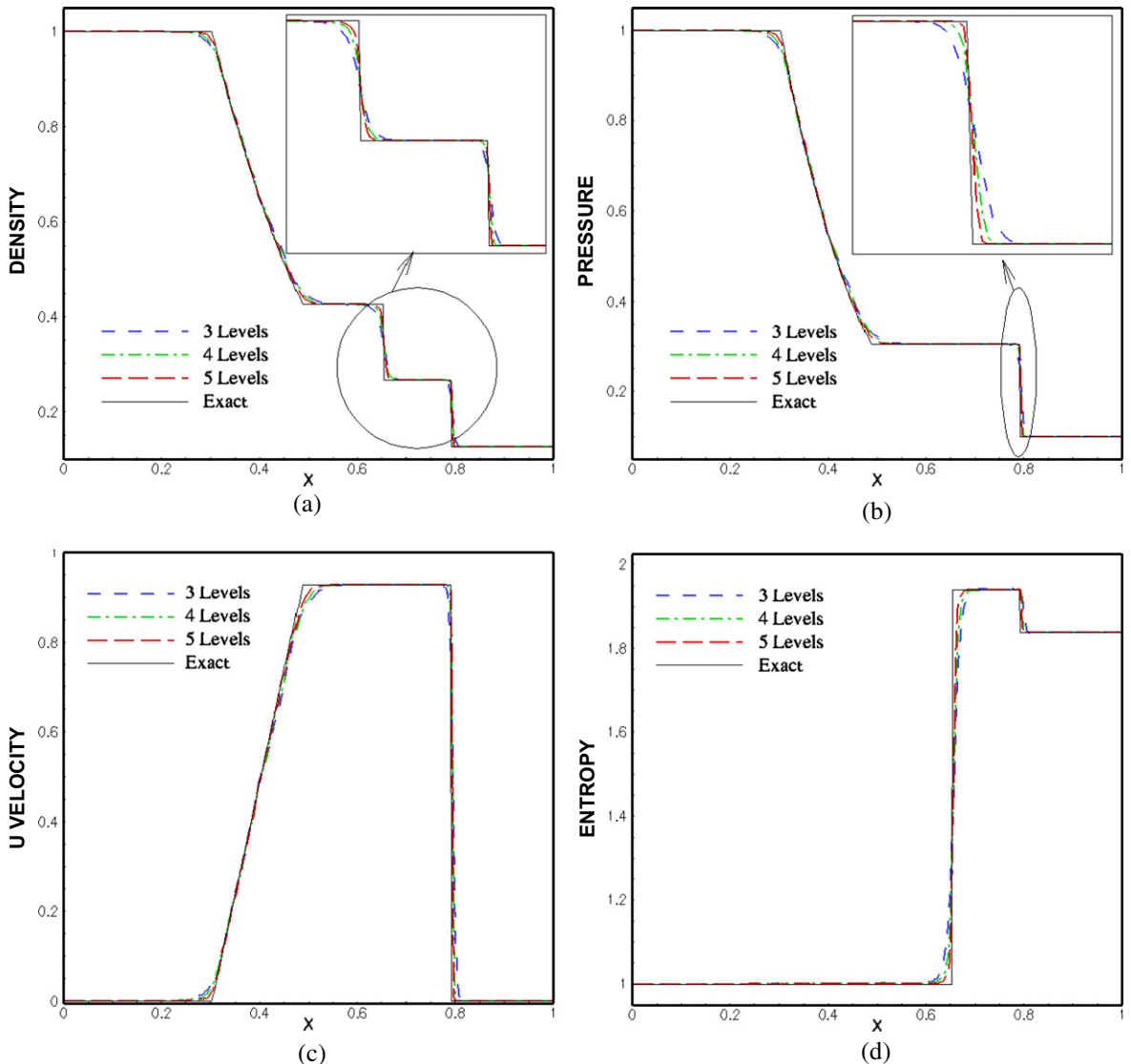


**Fig. 4.** Plots of (a) density, (b) pressure, (c) velocity (d) entropy for Sod's shock tube problem with pressure ratio  $\frac{p_2}{p_1} = 10$ .

Furthermore, in addition to the above refinement criterion, a layer of buffer cells are provided at the fine-coarse mesh boundary to ensure that the discontinuities are confined well within the fine mesh level. Thus, in contrast to the refinement criteria developed in [8,7], the criterion adopted in this work neither requires data storage at different time levels nor involves complex interpolation at different grid patches/levels.

#### 4.3. Computing ENO based numerical flux at the mesh interface

Several unstructured mesh-based ENO schemes have been developed in the past [12,1] but such schemes vary in complexity depending on the grid structure [13]. Cecil et al. [13] have developed an efficient scheme to construct ENO-based fluxes by identifying ghost points at the mesh interface. The ghost points in turn derived their flow properties from higher-order ENO-based inter-

polation procedure. The success of this approach is largely dependent on a stringent restriction imposed on the the grid level difference between neighbor cells. In their approach, the neighbor cells and the neighbor of neighbor cells, both in the grid and in the diagonal directions, were prohibited from having more than one level difference. One may have to extend the restriction to many cells for higher-order schemes. In contrast, in the current approach only the neighbor cells along the grid directions are not allowed to have more than one level difference in grid level. The approach adopted in this work also uses ghost points to construct fluxes at the mesh interface. As mentioned before, since the fine-coarse mesh transitions are designed to lie away from significant gradients in the flow and occupy a lower-dimensional space, a (conservative) bilinear interpolation scheme is found to be adequate to obtain the values at these ghost points. Moreover, with bilinear interpolation, extension to three-dimensions is straightforward.

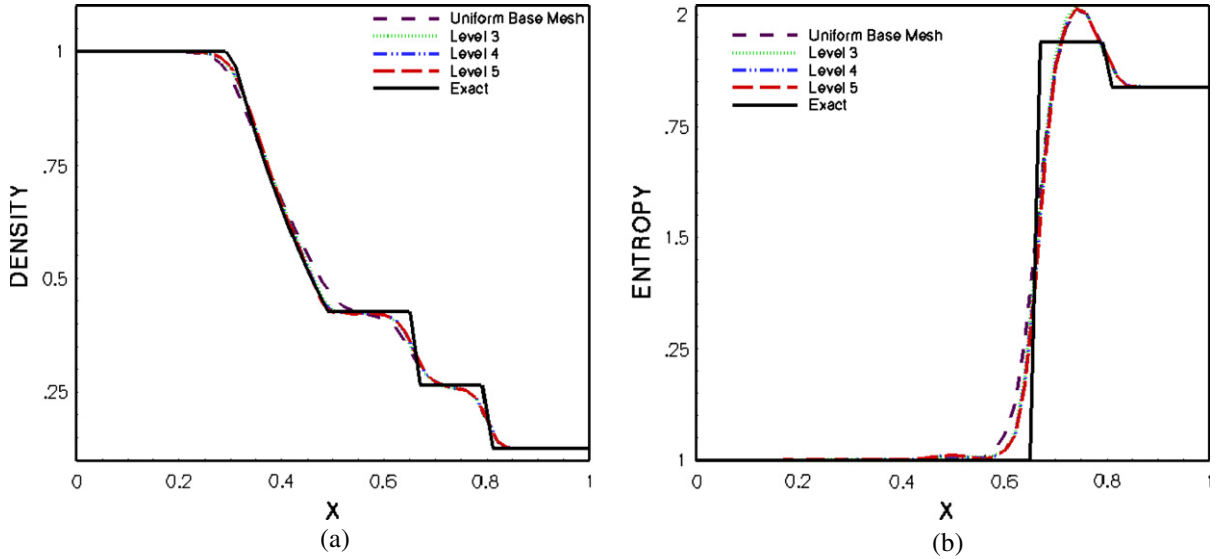


**Fig. 5.** (a) Density and (b) entropy plots for different levels of mesh refinement, for frozen mesh condition, for Sod's shock tube problem with pressure ratio  $\frac{p_2}{p_1} = 10$ .

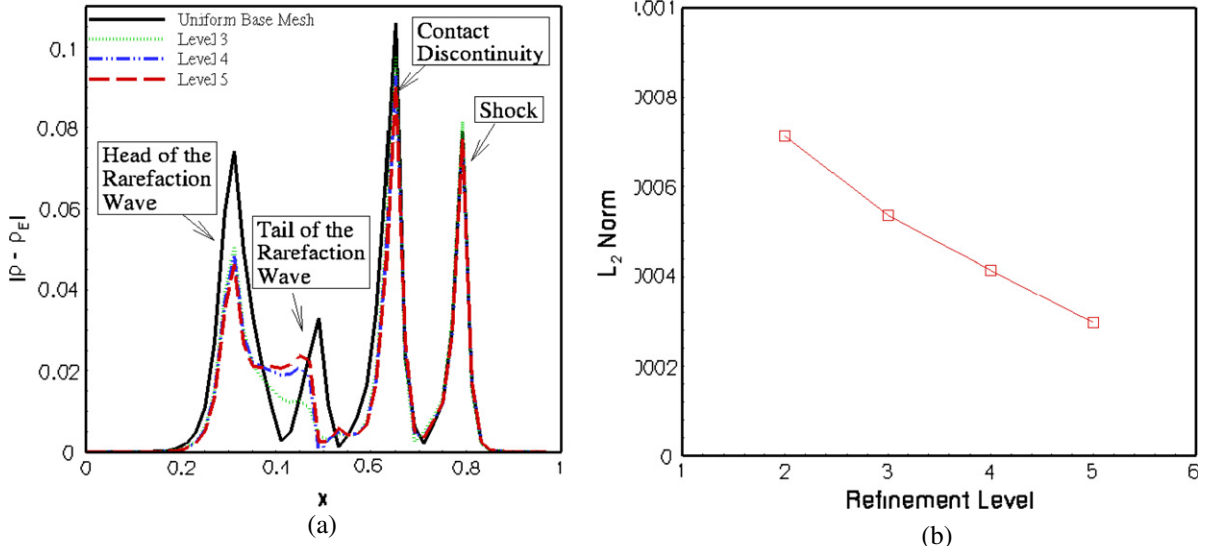


**Fig. 6.** Error distribution computed with respect to the exact solution for Sod's shock-tube problem with  $\frac{p_2}{p_1} = 10$  for different refinement levels, for frozen mesh condition: (a) Spatial variation of the absolute errors ( $\|\rho - \rho_{\text{EXACT}}\|$ ) (b)  $L_2(\rho)$ -norm of errors for density.

Details pertaining to the ENO-based flux construction approach for a uniform mesh distribution are discussed in [73,71]; the generic procedure for constructing the ENO-based numerical fluxes at the fine-coarse mesh interface is outlined below.

#### 4.3.1. Flux construction for a cell that is finer than its neighbor

Consider the typical case of the coarse-fine mesh boundary as shown in Fig. 3. In Fig. 3, cell P is at a level higher than its immediate neighbor cells W and N. The flux construction approach for the west face of cell P is illustrated:

1. The ghost points required for completing the ENO stencils are identified by comparing the status (divided or undivided) and refinement level of the neighboring cells. For cell P, three ghost points ( $GW_1, GW_2, GW_3$ ) on the west side, and two ghost points ( $GE_2, GE_3$ ) on the east side are required to complete the support stencil.
2. Once the ghost points are identified, the next step is to derive the fluxes and the flow properties for these ghost points. In order to construct the attributes for the ghost point  $GW_1$ , a non-conservative interpolation technique can either use points

**Table 1**

$L_2$ -norm of errors computed with respect to the exact solution for frozen mesh condition, for Sod's shock tube problem.

Refinement level	$L_2(\rho)$	$L_2(P)$	$L_2(u)$	$L_2(S)$
$\frac{P_2}{P_1} = 10$				
1	$4.07569 \times 10^{-3}$	$4.241 \times 10^{-3}$	$1.0865 \times 10^{-2}$	$1.2559 \times 10^{-2}$
3	$3.36566 \times 10^{-3}$	$3.503 \times 10^{-3}$	$1.049 \times 10^{-2}$	$1.08668 \times 10^{-2}$
4	$3.061 \times 10^{-3}$	$3.401 \times 10^{-3}$	$1.036 \times 10^{-2}$	$1.049 \times 10^{-2}$
5	$3.24515 \times 10^{-3}$	$3.379 \times 10^{-3}$	$1.031 \times 10^{-2}$	$1.038 \times 10^{-2}$
$\frac{P_2}{P_1} = 1000$				
1	$4.567 \times 10^{-2}$	557.8874	0.958	1478.400
3	$4.61 \times 10^{-2}$	557.9053	0.9774	1478.465
4	$4.613 \times 10^{-2}$	557.9093	0.9808	1478.475
5	$4.619 \times 10^{-2}$	557.9098	0.9819	1478.484

P, W, NW and N or points P, PS, W and NW for interpolation as shown in Fig. 3. Thus the choice for interpolation points is not unique. On the other hand, a conservative interpolation scheme uses a unique set of points for interpolation such as

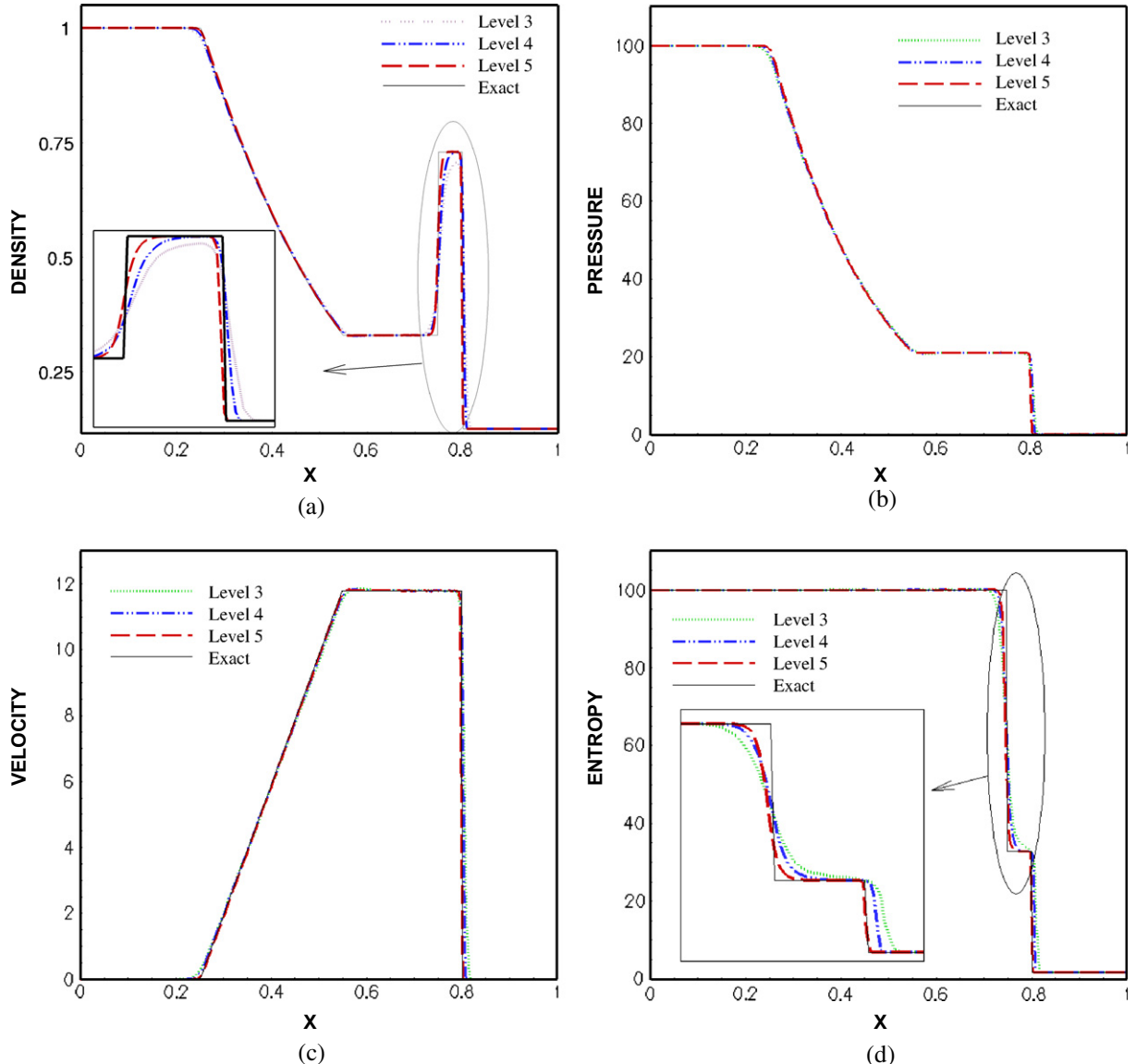


Fig. 7. Plots of (a) density, (b) pressure, (c) velocity (d) entropy for Sod's shock tube problem with pressure ratio  $\frac{P_2}{P_1} = 1000$ .

points W, NW, PI and N (Fig. 3). The point PI corresponds to the parent of cell P, and the flow attributes for point PI can be obtained by aggregating from its child cells i.e from cells P, PE, PS and PSE. Essentially, a conservative interpolation scheme uses points on the same level for interpolation. To clarify this procedure, a general scenario involving cells at different levels of refinement is presented in Fig. 3b. As shown in Fig. 3b, the fine-coarse grid interface involves grids with more than one level difference (along the diagonal direction). In such cases, points NWI, NI, PI and WI on the same level are used for interpolation. Fig. 3b shows how the flow properties and fluxes are aggregated from child cells to determine the flow properties at point NI. A similar procedure can be adopted to determine the flow properties and fluxes at points PI and WI. Identification of points of interpolation on the same grid level is straightforward. The procedure described above is repeated to define the flow attributes and fluxes for the remaining ghost points.

3. Once the attributes for the ghost points are determined, the construction of the flux  $f_{P_W}$  follows from the uniform mesh approach. Thus the method outlined in this section does not deviate much from the uniform mesh-based flux construction approach, and retains the simplicity of the ENO scheme flux construction for uniform meshes. The approach for constructing fluxes for other faces of cell P follow directly the procedure described above.

#### 4.3.2. Flux construction at the fine-coarse interface for cells abutting divided neighbors

If the cell under consideration is at a level lower than its immediate neighbor, the numerical flux corresponding to that face is not explicitly computed. With reference to Fig. 3b, cell W that abuts the fine mesh cells (P and PS) is at a level lower than its potential neighbors P and PS. Hence the flux crossing the mesh interface at the east face of cell W is not explicitly computed. Instead, the west fluxes for cells P and PS are summed to determine the net flux crossing the east face of cell W. Thus for the flux crossing the east face of cell W:

$$f_E = f_{P_W} + f_{PS_W},$$

where  $f_{P_W}$  and  $f_{PS_W}$  correspond to the fluxes crossing the west face of cells P and PS respectively. The fluxes  $f_{P_W}$  and  $f_{PS_W}$  are computed based on the procedure outlined above. Thus, explicit conservation of numerical fluxes at the interface of fine-coarse boundaries is achieved.

#### 4.3.3. Flux construction near the embedded interface

Since all cells in the narrow band of the levelset field corresponding to the embedded interface are refined uniformly to the same level, no special treatment is required for constructing the fluxes near the interface of the embedded object(s). Therefore, the Riemann solver based GFM technique developed for uniform mesh [55,54] can be directly applied near the interface of the embedded object(s).

## 5. Numerical examples

In this section several numerical examples are presented to demonstrate the robustness and versatility of the current approach. As mentioned before, the Euler equations (Eq. (1)) were solved using a third-order TVD-based Runge-Kutta scheme for time integration and third-order convex ENO scheme [41] for spatial discretization. The governing equations were non-dimensionalized based on free stream density  $\rho_\infty$ , pressure  $p_\infty$  and the sonic velocity  $a_\infty = \sqrt{\frac{p_\infty}{\rho_\infty}}$ . Unless otherwise stated, standard atmospheric

conditions are chosen to non-dimensionalize the governing equations. A suitable length scale is chosen depending on the dimensions of the immersed object. The CFL number was set to 0.6 for all of the simulations presented in this work. Numerical Schlieren images shown in this section were generated using the method outlined in [52] by defining the shade function  $v$  as:

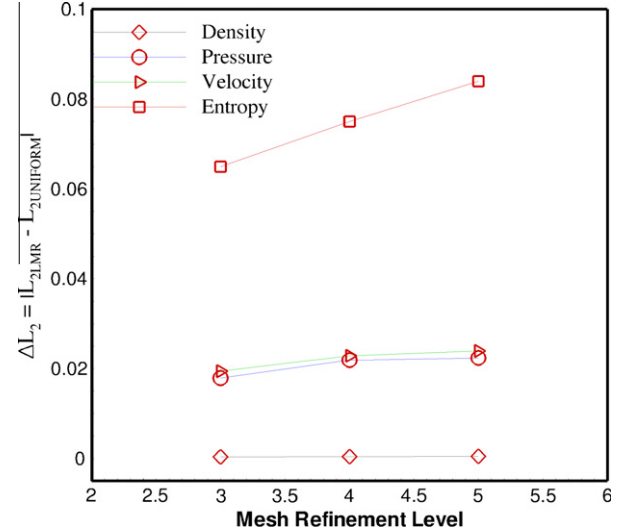


**Fig. 8.** Variation of  $|L_2_{MR} - L_2_{Uniform}|$  for different levels of mesh refinement with frozen mesh condition, for Sod's shock-tube problem with  $\frac{P_2}{P_1} = 1000$ .

**Table 2**

Initial conditions for the two-dimensional Riemann problem.

Configurations	Initial conditions
6	$x < 0.5; y > 0.5$ $\rho_2 = 2.0 P_2 = 1.0$ $u_2 = 0.75 v_2 = 0.5$ $x < 0.5; y < 0.5$ $\rho_3 = 1.0 P_3 = 1.0$ $u_3 = -0.75 v_3 = 0.5$
8	$x < 0.5; y > 0.5$ $\rho_2 = 1.0 P_2 = 1.0$ $u_2 = -0.6259 v_2 = 0.1$ $x < 0.5; y < 0.5$ $\rho_3 = 0.8 P_3 = 1.0$ $u_3 = 0.1 v_3 = 0.1$
19	$x < 0.5; y > 0.5$ $\rho_2 = 1.0 P_2 = 1.0$ $u_2 = -0.6259 v_2 = 0.1$ $x < 0.5; y < 0.5$ $\rho_3 = 0.8 P_3 = 1.0$ $u_3 = 0.1 v_3 = 0.1$

**Table 3**

$L_2(\rho)$ -norm of errors for density and OR for the two-dimensional Riemann problem.

Configurations	Time	Levels	$\delta_1$	$\delta_2$	$L_2 (\times 10^{-5})$	OR (%)
6	0.3	3	25.0	1000.0	$5.79 \times 10^{-5}$	26.42
		4	25.0	1000.0	$5.33 \times 10^{-5}$	13.03
		5	25.0	1000.0	$3.87 \times 10^{-5}$	9.1
8	0.25	3	1.0	1000.0	$9.077 \times 10^{-6}$	31.58
		4	1.0	1000.0	$8.204 \times 10^{-6}$	19.74
		5	1.0	1000.0	$6.278 \times 10^{-6}$	11.78
19	0.3	3	20.0	1000.0	$7.19 \times 10^{-5}$	29.9
		4	20.0	1000.0	$4.13 \times 10^{-5}$	16.1
		5	20.0	1000.0	$2.37 \times 10^{-5}$	5.71

$$v = e^{-\kappa \frac{\|\nabla p\|}{\| \nabla p \|_{\max}}}, \quad (26)$$

where  $\kappa$  is a problem-dependent coloring constant. For adaptive mesh calculations a representative measure of the computational load (memory and computational time), the percentage Occupancy Ratio (OR) (Eq. (27)) is computed. The OR is defined as the ratio of the maximum number of cells used in the solution

adaptive LMR calculation to the number of cells if a uniform fine mesh was used.

$$OR = \frac{MAX(NCELLS_{LMR}(t))}{NCELLS_{UNIFORMFINEMESH}} \times 100. \quad (27)$$

For problems involving moderate to strong shocks interacting with gas-gas or gas-solid interfaces, the threshold for the refinement

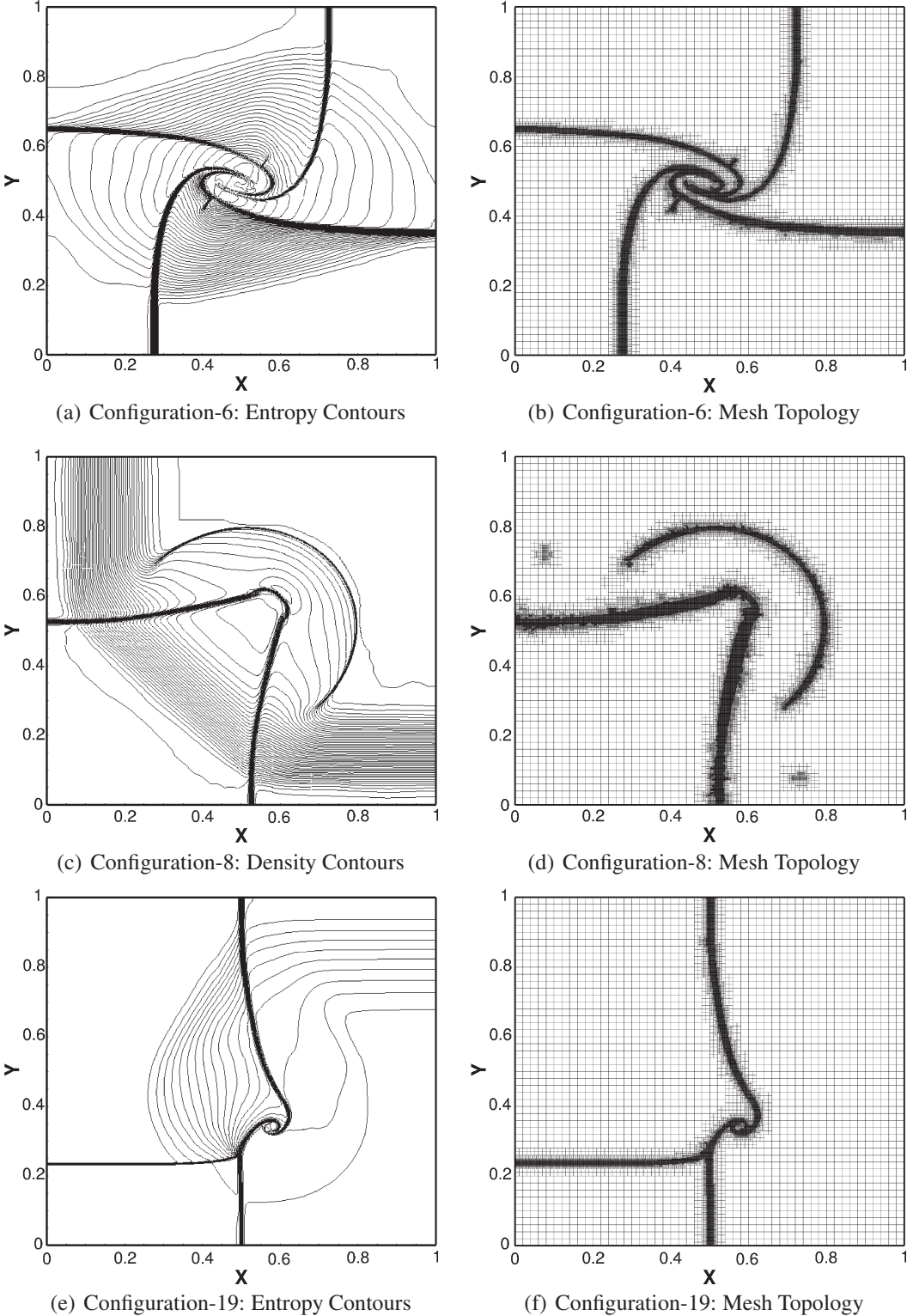


**Fig. 9.** Entropy contours (a and e), density contours (c) and mesh topology (b, d and f) for the two-dimensional Riemann Problem, with five levels of mesh refinement on a base mesh of size  $\Delta x_g = 0.02$ .

criteria were set in the range  $\delta_1 = \{1.0 - 100.0\}$  and  $\delta_2 = \{1.0 - 100000.0\}$  (arbitrarily large value). The threshold limit for  $\delta_2$  is set to arbitrarily large value if the resultant shock diffraction pattern does not contain weak structures and gradients that are under-resolved. For gas–water interface problems, due to very large difference in the stiffness of the material strength (impedance mismatch  $\rho a$ ), the threshold limits were set in the range  $\delta_1 = \{100.0 - 10000.0\}$  and  $\delta_2$  to an arbitrarily large value.

### 5.1. One-dimensional example

For the one-dimensional test case considered in this section, a computational domain corresponding to a shock tube of unit length and unit height was chosen. A base mesh of size  $\Delta x_g = 0.02$  was used for the simulations and the solutions were evolved with 3, 4 and 5 levels of mesh refinement corresponding to fine mesh size  $\Delta x_f = \frac{1}{200}$ ,  $\Delta x_f = \frac{1}{400}$  and  $\Delta x_f = \frac{1}{800}$  respectively.

#### 5.1.1. Sod's shock tube problem

The canonical Sod's shock tube problem is considered first. The initial conditions for the problem are as follows:

$$(\rho, P, u, \gamma) = \begin{cases} (1.0, 10.0, 0.0, 1.4) & \text{for } x < 0.5, \\ (0.125, 1.0, 0.0, 1.4) & \text{for } x \geq 0.5. \end{cases}$$

Pressure ratio across the discontinuity is fairly low,  $\frac{P_2}{P_1} = 10$ . The initial discontinuity results in a rightward moving shock wave and

contact discontinuity, and a leftward moving rarefaction wave. In this example no interface treatment technique was employed to resolve the contact discontinuity. The simulations were evolved to time  $T = 0.167$  units. Since the strengths of the shock wave and the expansion wave are low, the thresholds for the refinement criterion were set at  $\delta_1 = 1.0$  and  $\delta_2 = 100000.0$ . The solution obtained from the current simulations along with the exact solution are displayed in Fig. 4. As can be seen from the plots, the numerical solutions from the current calculations closely follow the exact solution. It was demonstrated in [16] that spurious reflected waves were observed when waves were made to pass through the fine-coarse mesh interfaces. Therefore, in order to characterize the impact of the interpolation procedures at the fine-coarse mesh boundaries, the mesh refinement was frozen after the first time step, prohibiting the mesh from adapting to the solution. This allows the shock wave, the contact discontinuity and the rarefaction wave to pass through the fine-coarse mesh boundaries and hence the interpolation errors generated at the fine-coarse mesh interfaces can be examined. Although the refinement criterion developed in this work prohibits the passage of strong discontinuities across the mesh interfaces, the intent of this analysis is to examine the errors generated in the limiting case of a shock wave passing through the mesh interface.

The density and the entropy plots for the frozen mesh condition are displayed in Fig. 5. Once the shock and the contact discontinuity move into the coarse mesh region, they assume a diffusive profile (corresponding to the size of the coarse mesh  $\Delta x_g$ ). The plots

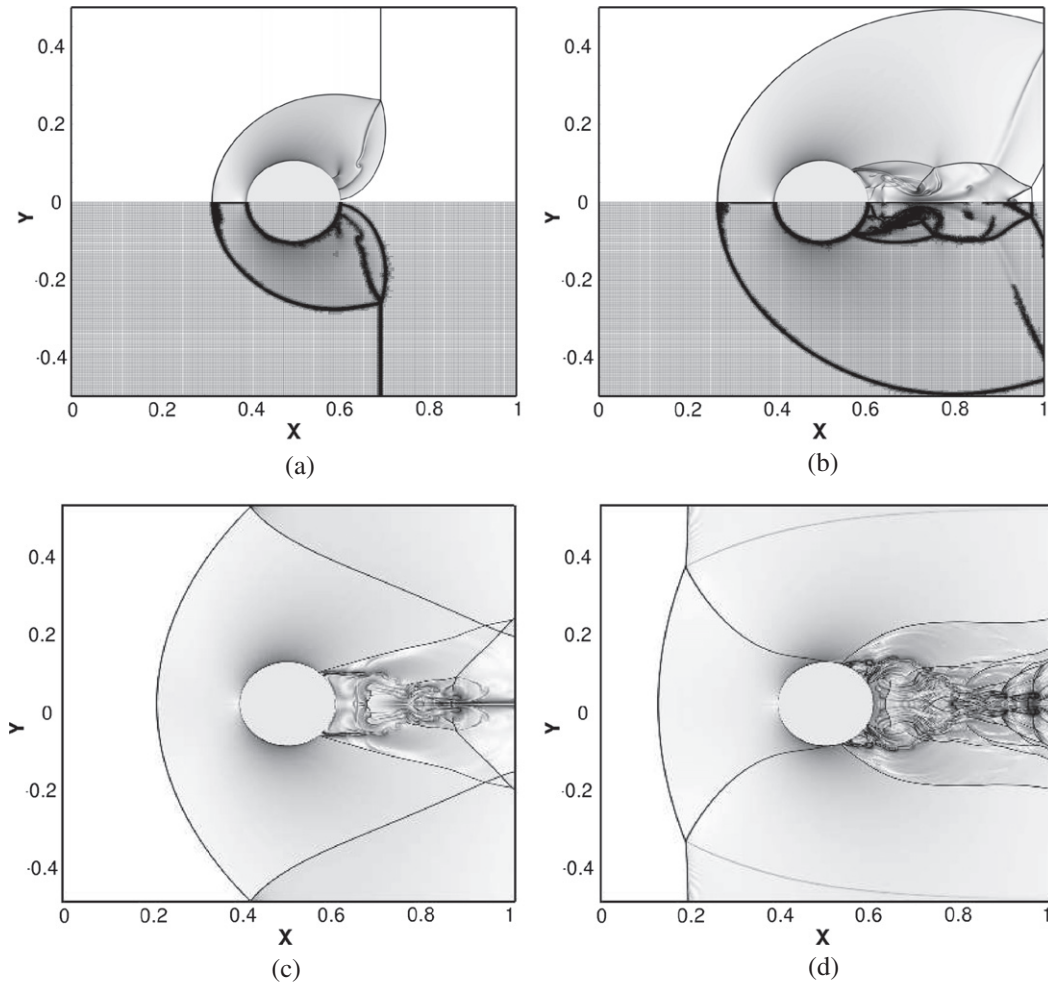


**Fig. 10.** Numerical Schlieren image at different instants in time, for a Mach 2.81 shock wave diffracting off a stationary cylindrical obstacle, computed on a base mesh of size  $\Delta x_g = \frac{1}{300}$  with four levels of mesh refinement: (a)  $T = 0.314 \mu\text{s}$ ; (b)  $T = 0.612 \mu\text{s}$ ; (c)  $T = 1.1 \mu\text{s}$ ; (d)  $T = 2.4 \mu\text{s}$ .

are in good agreement with the uniform mesh solutions. The spatial variation of the absolute errors ( $\epsilon = |\rho_{\text{Numerical}} - \rho_{\text{Exact}}|$ ) and the  $L_2$ -norm of errors for density (also computed with respect to the exact solution), for different levels of mesh refinement are plotted in Fig. 6. As can be seen from Fig. 6a, no spurious reflected waves from the mesh interface are observed. The errors near the region occupied by the shock and the contact discontinuity are consistent with the prediction made by the uniform mesh solution. However, the errors near the head and the tail of the rarefaction waves are significantly lower than the errors generated by the uniform mesh solution. This is because of the presence of the frozen patch of fine mesh around the initial discontinuity (i.e. at  $x = 0.5$ ) that partly spans the region occupied by the tail of the rarefaction wave. Furthermore, in the region occupied by the shock and the contact discontinuity, the error decreases with increase in mesh refinement level. This is counter-intuitive, particularly for higher levels of mesh refinement which involve interpolations across different grid levels. The reason for this can be attributed to the way in which the

solution is evolved in the LMR framework. Unlike AMR schemes, the flow field is evolved at all grid points in a single sweep for a given time step. As a result, the smallest time step determined by the size of the fine mesh cell is enforced for the global time update. With the increase in mesh refinement levels, smaller time steps are enforced globally and hence the interpolation errors are mitigated. The  $L_2$ -norm of errors for density, computed for both the frozen mesh condition and the LMR solution, plotted in Fig. 6b clearly confirm this fact (the errors decrease with increase in mesh refinement levels).

Next a stronger shock was simulated with pressure ratio  $\frac{P_2}{P_1} = 1000$ . The solution obtained from the current simulations for different levels of mesh refinement are displayed in Fig. 7. The threshold for the refinement criteria are the same as in the previous case, and the solutions are evolved to time  $T = 0.021$  units. The numerical solutions tend towards the analytical solutions with increase in mesh refinement level. Similar to the previous case, the mesh evolution was frozen after the first time step, and  $L_2$ -norm of

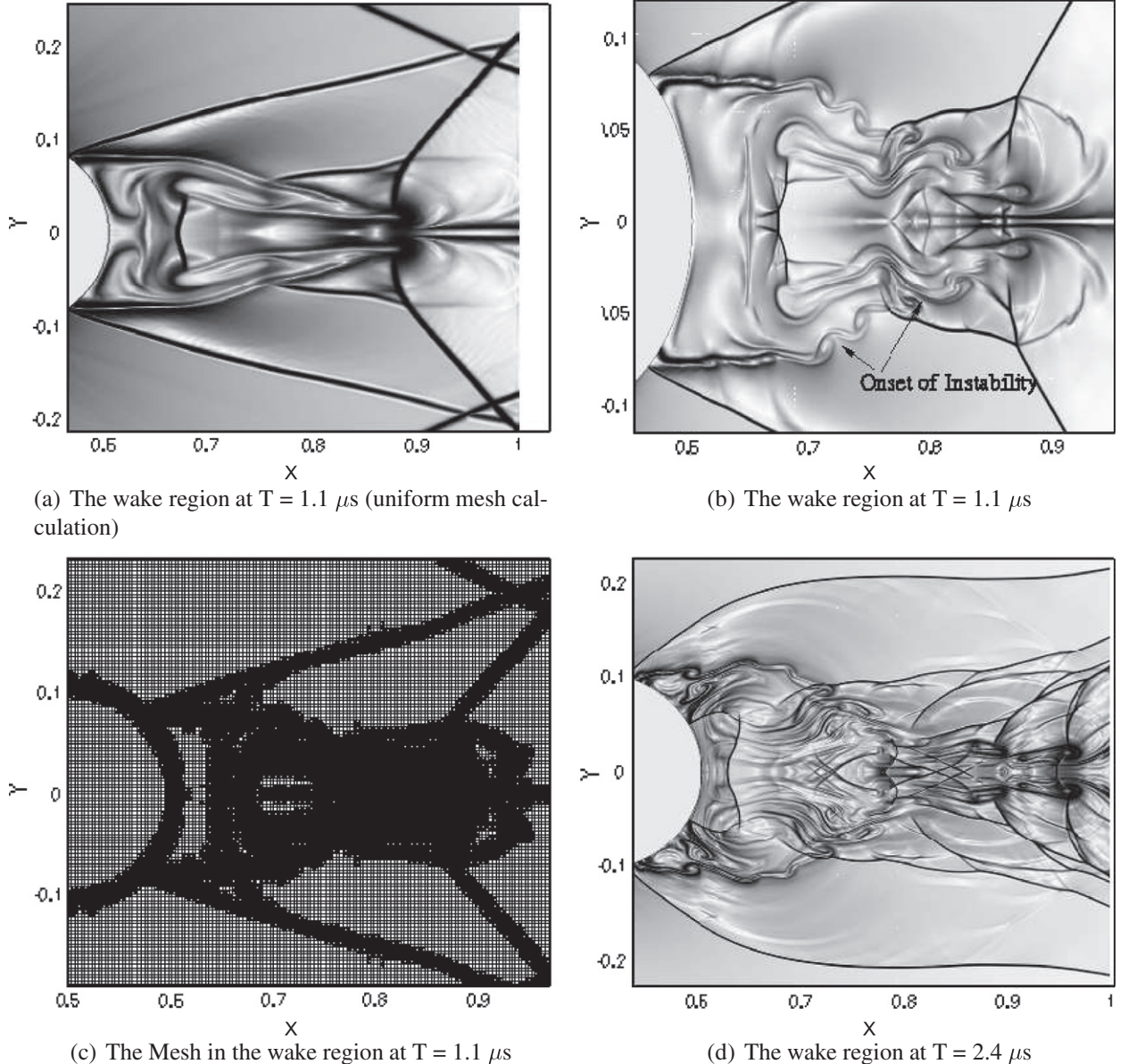


**Fig. 11.** Enlarged view of the wake region at two different instants in time: (a) Uniform mesh calculation with  $\Delta x = \frac{1}{800}$  at  $T = 1.1 \mu\text{s}$ ; (b) LMR calculation at  $T = 1.1 \mu\text{s}$ ; (c) Mesh topology in the wake region at  $T = 1.1 \mu\text{s}$ ; (d) LMR calculation at  $T = 2.4 \mu\text{s}$ .

the errors computed with respect to the exact solution are displayed in Table 1. The errors incurred, although large for some variables, are comparable for different levels of mesh refinement. The difference in the  $L_2$ -norm of the errors computed for the uniform mesh solution and the LMR solution with frozen mesh condition, are plotted in Fig. 8. In contrast to the previous case, the  $L_2$ -norm of the errors increase with mesh refinement level. Thus, as one would expect, it can be inferred from the above two examples that the errors incurred due to interpolation across shock waves increase with shock strength. Such errors can be averted if shocks and other strong discontinuities are contained well within the fine mesh level, by inhibiting their movement across fine-coarse mesh boundaries.

## 5.2. Two-dimensional examples

### 5.2.1. Two-dimensional riemann problem (TDRP)

The two-dimensional Riemann problems (TDRP) consist of a combination of one-dimensional wave patterns, giving rise to 19 different configurations [39]. As one can construct numerous elementary wave patterns, it is not possible to derive an analytical solution for the TDRPs. However, the solution for each configuration of the TDRP is well established and has been widely used to test several high resolution numerical schemes [39,36]. In this work, three different configurations (6, 8 and 19) of the TDRP are considered, to test the accuracy and performance of the LMR scheme in the two-dimensional set up. The initial conditions for each configuration correspond to a constant state in each quadrant of a computational domain of unit length and unit height. Neumann conditions are applied at the domain boundaries. The initial conditions corresponding to each configuration are listed in Table 2.

Shown in the figure are the density and entropy contours, and the mesh topology for five levels of mesh refinement on a base mesh of size  $\Delta x_g = 0.02$ . The details of the numerical solutions are displayed in Table 3. The  $L_2$ -norm of errors displayed in the table are computed by comparing the solution with the corresponding uniform fine mesh calculations (with  $\Delta x = \frac{\Delta x_g}{2^{k-1}}$ ;  $k = 3, 4$  and 5). As expected the  $L_2$ -norm of errors decrease with mesh refinement, indicating that the solutions obtained from the LMR calculations concur with the corresponding fine mesh calculations. In addition,

**Table 4**

Timing analysis for a Mach 2.81 shock negotiating a stationary cylindrical obstacle, for different levels of refinement with  $\Delta x_f = \frac{1}{800}$

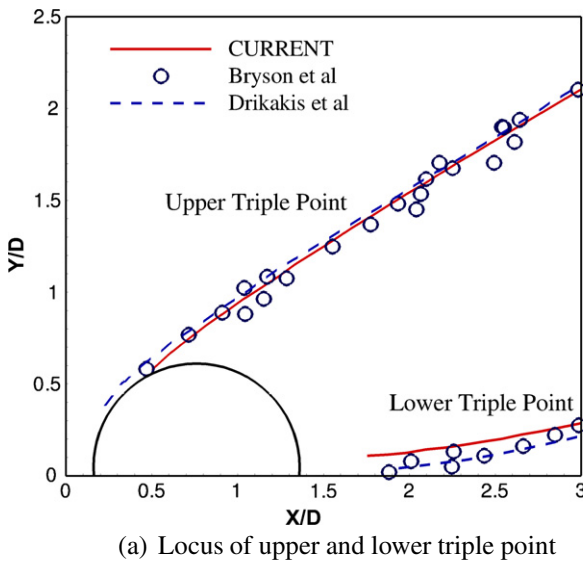
Ref. levels	$\Delta x_g$	CPU time (in %)	OR	$L_2(\rho)$
1	0.0025	100	100	–
3	0.005	36.6	46.72	$3.918 \times 10^{-5}$
4	0.01	39.15	46.1725	$4.198 \times 10^{-5}$
5	0.02	60.98	47.286	$4.746 \times 10^{-5}$
6	0.04	163.8	51.88	$5.439 \times 10^{-5}$

the OR shown in Table 3, decreases with increase in mesh refinement level. In particular, the OR for configuration 19 is 5% (only 5% of the computational domain is occupied by fine mesh cells). Thus, with the current formulation of the tree-based LMR scheme, substantial savings in computational resources can be attained. The mesh topology shown in Fig. 9 indicate that the refinement criterion developed in this work is effective in identifying and following the important features such as shocks and entropy layers.

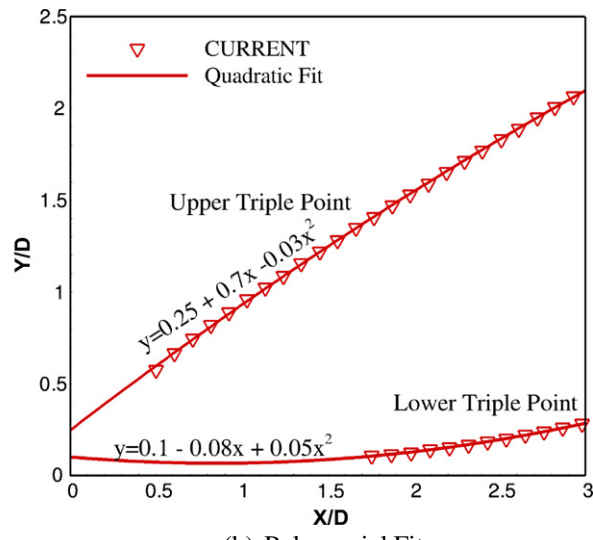
### 5.2.2. Diffraction of mach 2.81 shock wave negotiating a stationary cylindrical obstacle

First in the series of shock-interface interaction computations presented in this work, is the interaction of a planar shock wave with stationary cylindrical obstacle. Due to the symmetry of the problem, only one-half of the problem was modeled using a symmetry condition at the bottom wall. Reflective boundary condition for the top wall and Neumann condition for outlet were imposed. At the inlet, a Dirichlet condition was enforced. The semi-circular obstacle with radius 0.105 mm was positioned at  $x = 0.5$  mm and  $y = 0.0$  mm in a computational domain of size 1 mm  $\times$  0.5 mm. The initial discontinuity was located at  $x = 0.385$  mm so that the sharp discontinuity relaxes to a numerical shock profile before impacting the obstacle.

**5.2.2.1. High resolution calculation.** A fine base mesh of size  $\Delta x_g = \frac{1}{300}$  with four levels of mesh refinement was selected (an effective resolution of 3 million grid points when uniformly spaced throughout the domain).  $\delta_1$  and  $\delta_2$  were set at 10.0 and 250.0 respectively. The results from the current calculations are presented in Fig. 10. The problem has been extensively investigated in the past and diffraction patterns observed are well documented



(a) Locus of upper and lower triple point



(b) Polynomial Fit

**Fig. 12.** (a) Comparison of locus of upper and lower triple point with experimental [68] and numerical [21] predictions. (b) A parabolic fit for the locus of the upper and lower triple point.

[5,11,66,53,76,57,54]. As pointed out in [5], the initial interaction of the planar shock with the cylinder is a regular reflection with the shock reflecting normally along the axis of symmetry. This initial interaction of shock wave forms a bow shock that is typical of shock interacting with bluff bodies. The reflected shock begins traversing the cylinder before transitioning to a Mach reflection. The

Mach reflection consists of the incident shock, the reflected shock, Mach stem and slip-line (Fig. 10a). The slip-line emanating from the Mach stem is clearly visible in Fig. 10a. In addition, the roll up of slip-line is also captured accurately. The curved Mach stem travels down the cylinder and interacts with the shock system from the symmetrical part of the cylinder to form the wake region

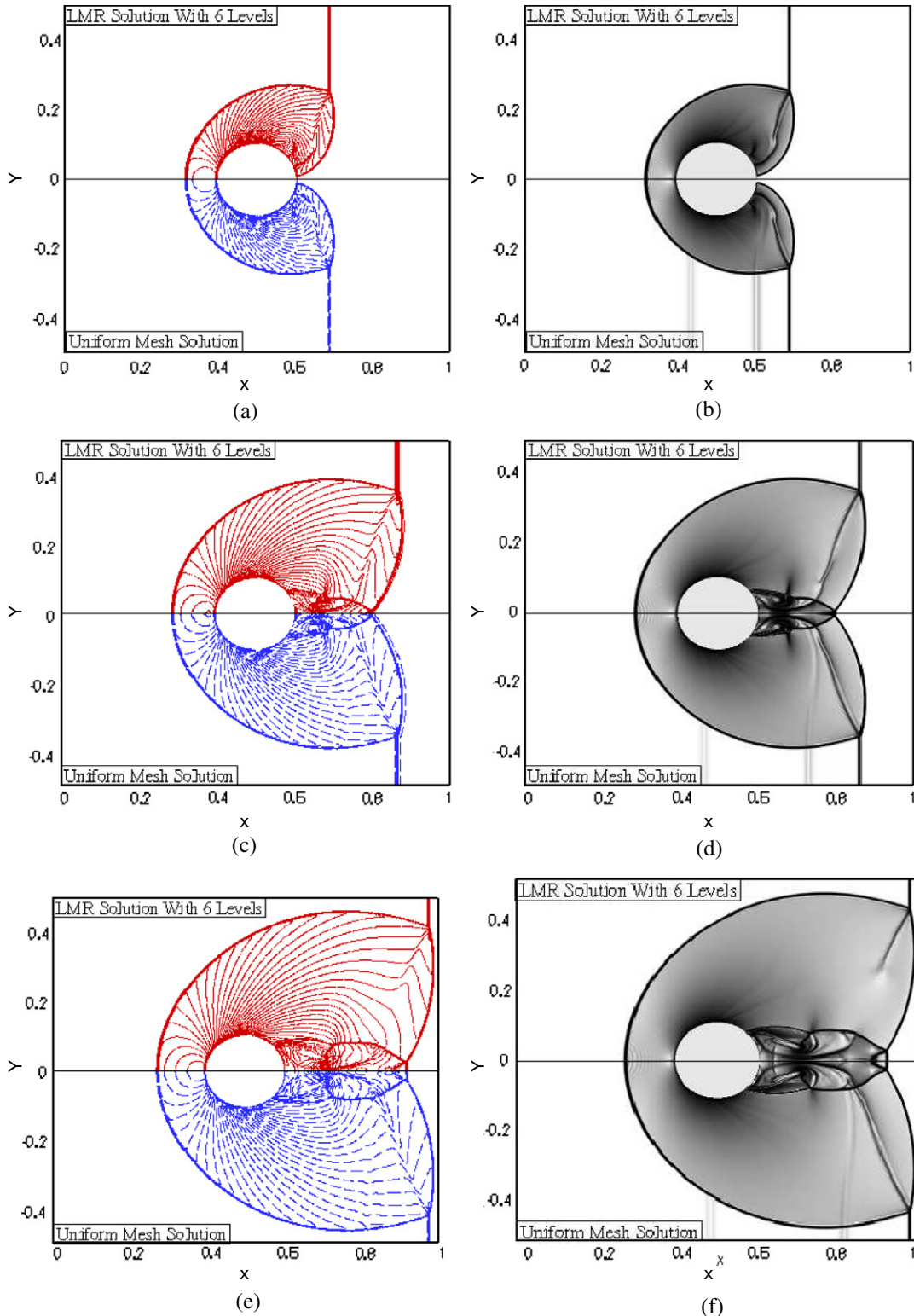


**Fig. 13.** Comparison of density contours ((a), (c) and (e)) and numerical Schlieren image ((b), (d) and (f)) for LMR-based calculation with six levels of mesh refinement, with the uniform fine mesh computations (with  $\Delta x = \frac{1}{800}$ ) at different instants in time: (a) and (b) at  $T = 0.314 \mu\text{s}$ , (c) and (d) at  $T = 0.47 \mu\text{s}$  and (e) and (f) at  $T = 0.565 \mu\text{s}$ .

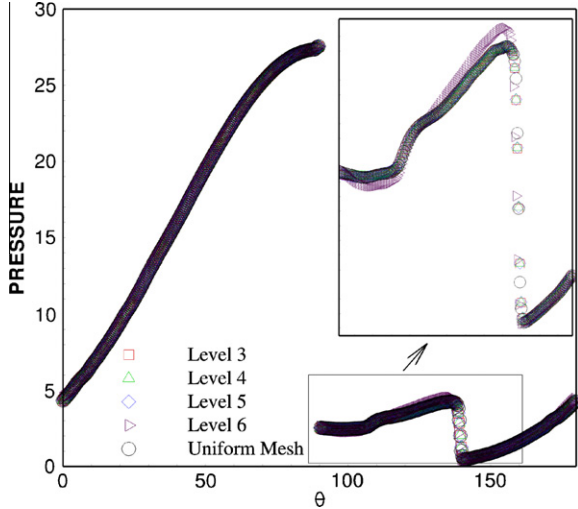


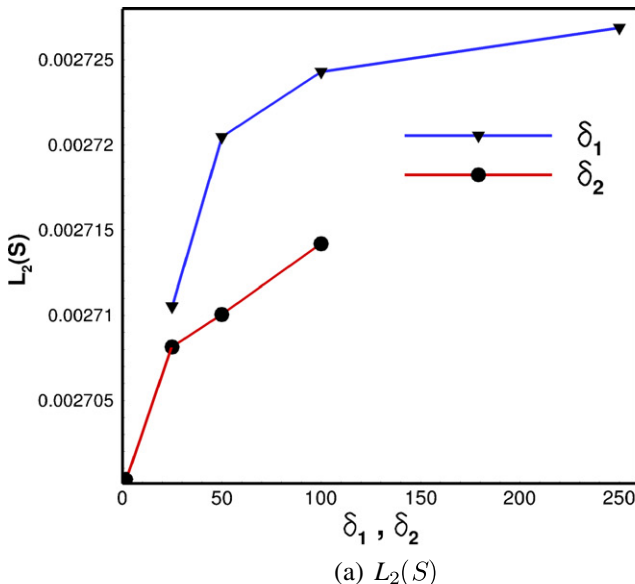
**Fig. 14.** Comparison of pressure distribution on the surface of the cylinder for different levels of mesh refinement at time  $T = 0.565 \mu\text{s}$ .

(Fig. 10b–d). The enlarged view of the wake region at two different instants in time are displayed in Fig. 11. In Fig. 11b, the onset of Kelvin-Helmholtz instability in the wake region can be seen. For the sake of comparison, the enlarged view of the wake region from a uniform mesh calculation ( $\Delta x = \frac{1}{800}$ ) is presented (Fig. 11a). As shown in Fig. 11a and b, the onset of instability is only apparent with sufficiently fine mesh refinement. The subsequent development of the instability at a later instant in time ( $T = 2.4 \mu\text{s}$ ) is shown in Fig. 11d. Fig. 11c shows the enlarged view of the mesh in the wake region (at  $T = 1.1 \mu\text{s}$ ). The mesh adaptation is excellent and closely follows the delicate contours of vorticity, slip-lines and the shock systems in the wake region. The OR computed for this simulation is 8.7%. In Fig. 12, the locus of upper and lower triple point are plotted with experimental [11] and numerical [21] predictions. The trends are in excellent agreement. In Fig. 12b, a perfect parabolic fit is obtained which is consistent with the predictions made in [53]. Furthermore, the angle, made by the locus of the upper triple point with the horizontal is  $33^\circ$  which is the value reported in the experimental observations in [35].

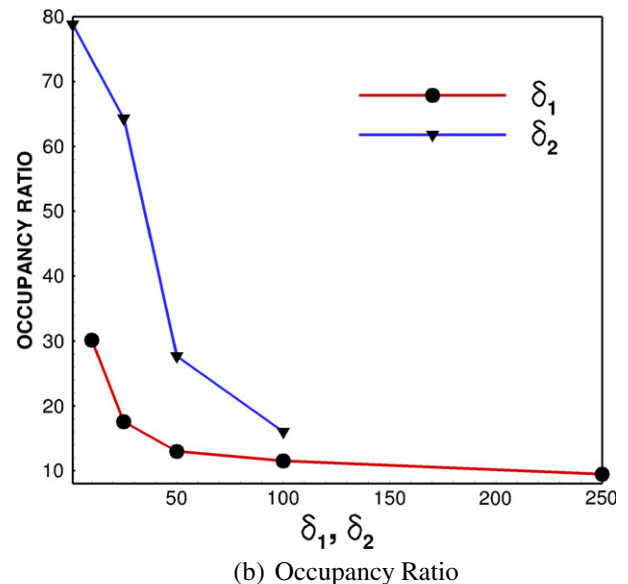
**5.2.2.2. Computational time study.** As the diffraction patterns are rich with features typical of shock-interface interaction phenomena, the problem is selected as a prototype for performing timing analysis. The simulations were evolved to time  $T = 6.28 \mu\text{s}$ . The refinement criteria for the LMR calculations were set to  $\delta_1 = 10.0$  and  $\delta_2 = 25.0$ . For a representative measure of computational time, the percentage CPU time ratio was computed and compared to the CPU time taken by the uniform fine mesh calculation ( $\Delta x = \frac{1}{800}$ ). The solutions were evolved for four different (3–6) levels of mesh refinement while maintaining the size of the fine mesh cells constant, i.e.  $\Delta x_f = \frac{1}{800}$  and  $\Delta x_g = \Delta x_f \times 2^{k-1}$ , where  $k$  is the refinement level. The details from the current calculations are displayed in Table 4. As is evident from the table, although the OR remains almost constant, the % CPU time increases with increase in the levels of mesh refinement. Particularly for the case with six levels of mesh refinement (on a coarse base mesh of size  $\Delta x_g = 0.04$ ), the CPU time is well above 100%. The reason for this increase in CPU time can be attributed to a coarse base mesh used in the calculation, and the interpolations performed over different grid levels at the fine-coarse mesh boundary. Hence, for fast computations with a given OR, the recommended limit on the mesh refinement level is 5. Furthermore, considering speed and accuracy of the calculation, four levels of mesh refinement can be chosen as an optimal refinement level.

In Fig. 13, the LMR-based solution with six levels of mesh refinement (top portion of the figure) are compared with the corresponding fine mesh calculations with  $\Delta x = \frac{1}{800}$  (bottom reflected portion of the figure). As can be seen from the figure, the shock locations and the wake regions are resolved accurately. The pressure distribution on the surface of the cylinder are plotted in Fig. 14. As the interface is always maintained at the finest level, the pressure distribution for different levels of mesh refinement are in excellent agreement with the uniform mesh solution.

**5.2.2.3. Sensitivity to refinement criteria.** Next, the sensitivity of the solution to the refinement criteria is examined. For this purpose, the calculations were repeated on a base mesh of size  $\Delta x_g = 0.01$  with four levels of refinement. To examine the impact of  $\delta_1$  on the solution, simulations were performed for a range of values of  $\delta_1$  with  $\delta_2$  held constant (at arbitrary large value). A similar approach was adopted to examine the effect of  $\delta_2$  on the solution.



(a)  $L_2(S)$



(b) Occupancy Ratio

**Fig. 15.** Sensitivity of the solution to the refinement criteria: (a)  $L_2(S)$ -norm of errors for entropy (b) Percentage mesh occupancy ratio.

The two sets of data are presented in Fig. 15. As is apparent from the figure, with the decrease in the threshold limit, the  $L_2(S)$ -norm of error decreases with increase in the occupancy ratio. The trend

observed with respect to the  $L_2(S)$ -norm of error for  $\delta_1$  and  $\delta_2$  are similar. This is because the primary shock systems are resolved with decrease in threshold limit. In contrast, the trend observed

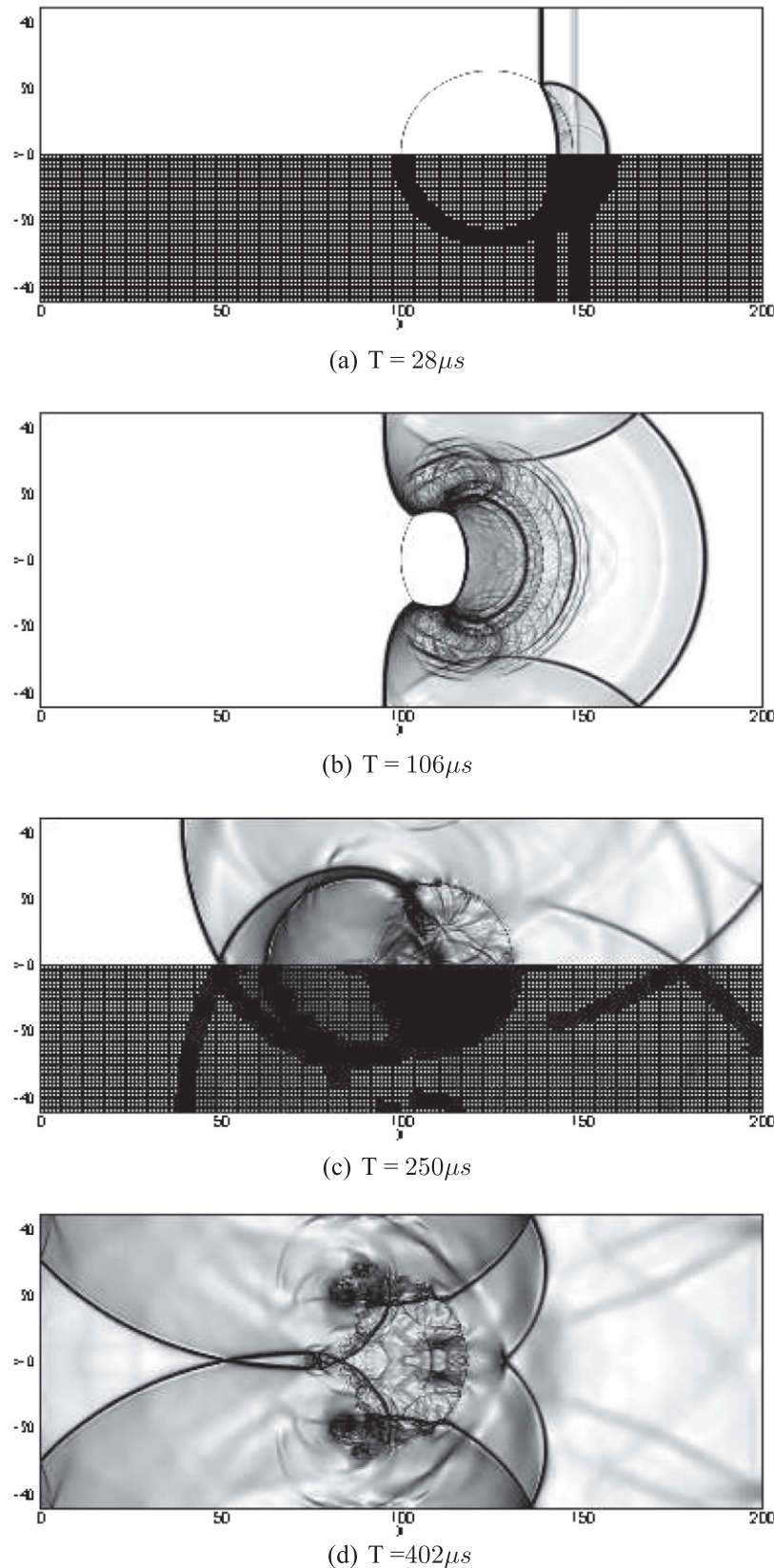


**Fig. 16.** Snapshots of mesh evolution and numerical Schlieren image for a planar shock (Mach 1.22) interacting with  $R_{22}$  cylindrical bubble at different instants in time.

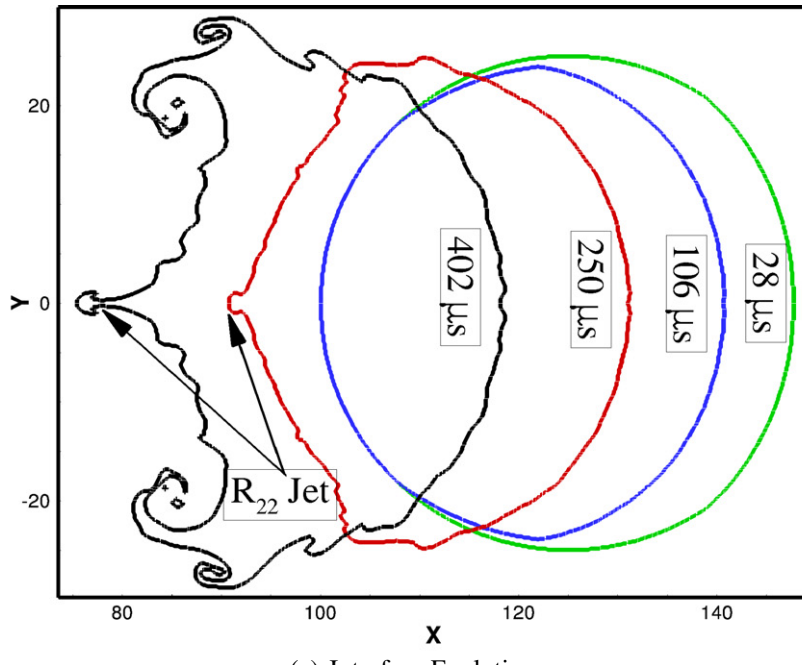
with the occupancy ratio differ significantly from one another. This is because, with the decrease in the threshold limit for  $\delta_2$ , weak features/gradients are accentuated and resolved to the finest level. Thus to balance accuracy and speed of the calculation, the suggested range for the threshold limits,  $\delta_1$  and  $\delta_2$ , are  $\delta_1 \Delta x_g \approx \left\{ \Delta x_g - \frac{1.0}{\Delta x_g} \right\}$  and  $\delta_2 \Delta x_g \approx \{2.5 \Delta x_g - 100 \Delta x_g\}$  respectively, where  $\Delta x_g$  is the size of the global base mesh.

### 5.2.3. Mach 1.22 shock interacting with cylindrical ( $R_{22}$ ) gas bubble

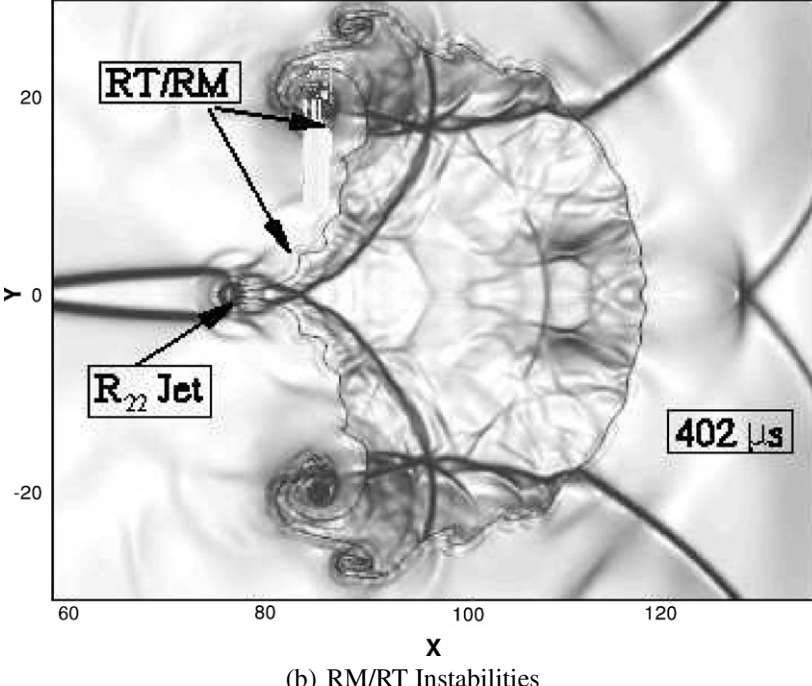
High resolution computation of a weak shock (Mach 1.22) interacting with a cylindrical  $R_{22}$  bubble in air is considered. The initial planar shock is located at  $x = 155$  mm in a computational domain

of size  $200 \text{ mm} \times 44.5 \text{ mm}$ . The cylindrical bubble of diameter 50 mm is initially located at  $x = 125$  mm. Due to the symmetry of the problem only one half of the bubble is modeled. The initial conditions for the shocked and un-shocked air along with the conditions inside the bubble are given below:

$$(\rho, P, u, v, \gamma) = \begin{cases} (1.3764, 1.5698, -0.394, 0.0, 1.4) & x \geq 155.0 \\ (1.0, 1.0, 0.0, 0.0, 1.4) & x < 155.0 \\ (3.15385, 1.0, 0.0, 0.0, 1.249) \sqrt{(x - 125)^2 + (y)^2} & \leq 50 \end{cases}$$



(a) Interface Evolution



(b) RM/RT Instabilities

**Fig. 17.** Enlarged view of the (a) interface topology at different instants in time and (b) instabilities occurring at the interface, for a Mach 1.22 shock interacting with  $R_{22}$  cylindrical bubble.

The right end of the domain is prescribed with the Dirichlet condition corresponding to the post-shocked air. The left end of the domain is prescribed with Neumann conditions, the top and bottom portions of the domain with reflective conditions. The simulations are evolved with a base mesh  $\Delta x_g = 1.0$ , with four levels of mesh refinement (corresponding to 800 points per diameter). Due to the rather weak shock, the thresholds for the refinement criterion are set at  $\delta_1 = 0.01$  and  $\delta_2 = 0.01$ .

Since the impedance offered by the  $R_{22}$  bubble is comparable to that of post-shocked air ( $(\rho c)_{R_{22}} - (\rho c)_{air} \approx 0.09$ ), the shock-interface interaction resolves into a transmitted shock wave and a reflected shock wave. As the speed of sound is greater in the air medium, the incident shock wave travels faster than the weak refracted wave system (Fig. 16a and b). Furthermore, the velocity of air behind the incident shock wave is greater than the velocity behind the transmitted shock wave inside the bubble. As pointed out in [3], this velocity difference introduces a counter-clockwise torque on the surface of the bubble which later develops into a Kelvin-Helmholtz (KH) instability. In addition, the interface is also subjected to Richtmyer-Meshkov (RM) instability due to the interaction of the shock system with the curved front of the bubble. The unstable interface eventually rolls up to form vortices and fragments on the interface (Fig. 16c and d). To accurately

resolve these vortical structures generated on the interface, extremely fine grid resolution is required as the sharp interface calculations are devoid of numerical diffusion phenomena that are common with approaches such as the diffuse interface approaches [14,44]. As shown in Fig. 16d and Fig. 17b, with the current LMR scheme the vortical patterns and the shock systems are captured. Also seen in the figure is the  $R_{22}$  jet formed in the trailing edge of the bubble. As pointed out in [3], due to the formation of the compression wave inside the bubble and the focussing effect of the incident shock wave, there is a steep rise in the pressure at the trailing edge of the bubble. This steep rise in pressure causes the onset of a jet at the trailing edge of the bubble. In Fig. 17, the topology of the interface at different instants in time are plotted. The figure clearly shows the instabilities and the  $R_{22}$  jet formed on the interface. The dynamic adaptation of the mesh is apparent from Fig. 16. The occupancy ratio computed for this simulation is 17.3%.

#### 5.2.4. Shock interacting with spherical water droplet

Shock-droplet interaction is a typical multi-material problem with wide range of applications such as corrosion effects on turbine blades, fuel-coolant interaction in nuclear reactors, ablation of space vehicles during re-entry, etc. [15]. Effect of planar shock

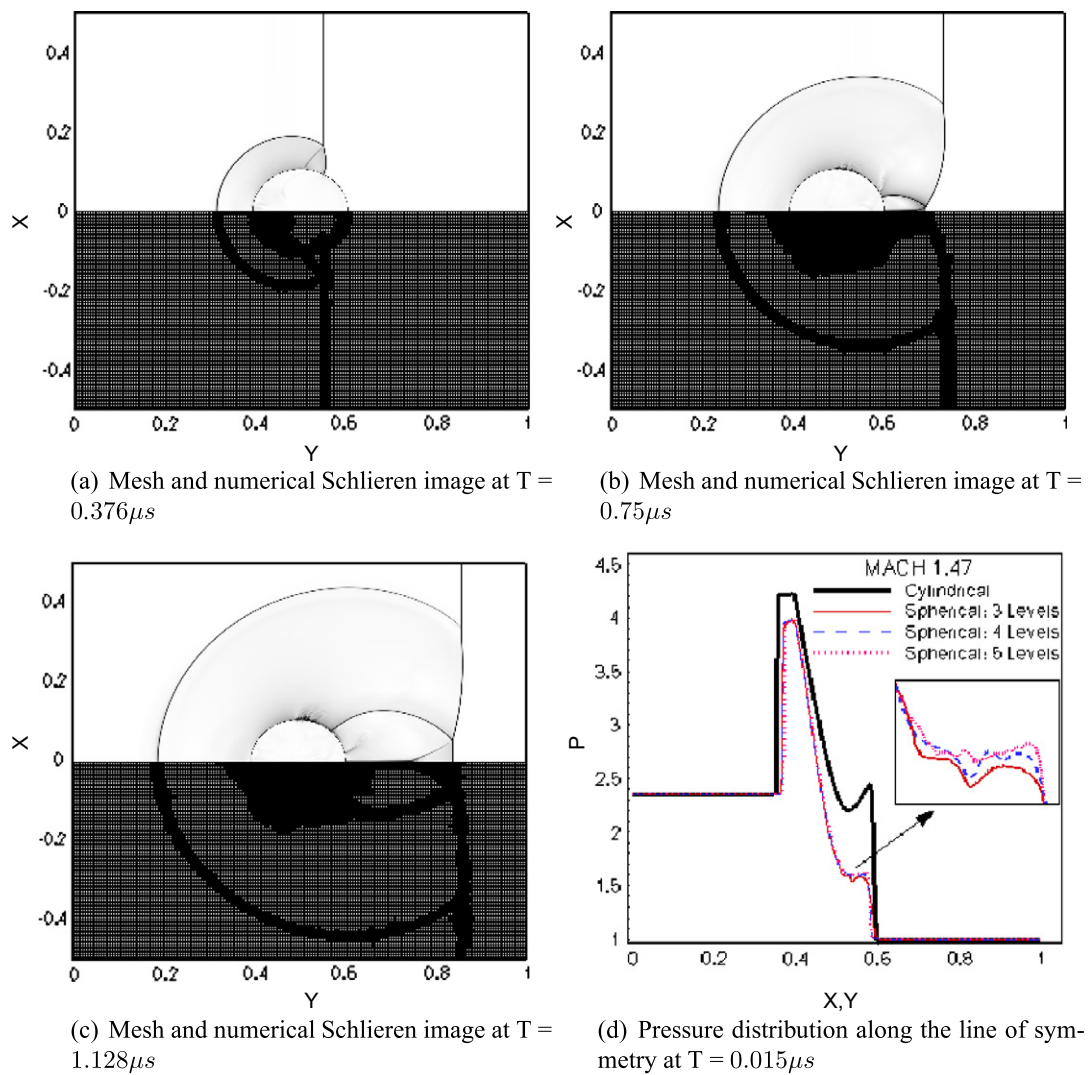


**Fig. 18.** Mach 1.47 shock interacting with spherical water droplet: (a), (b) and (c) Snapshots of mesh evolution and numerical Schlieren image at  $T = 0.376\mu s$ ,  $T = 0.75\mu s$  and at  $T = 1.128\mu s$  respectively, computed on a base mesh  $\Delta x_g = \frac{1}{200}$  with five levels of mesh refinement; (d) Pressure distribution along the line of symmetry at  $T = 0.015\mu s$ .

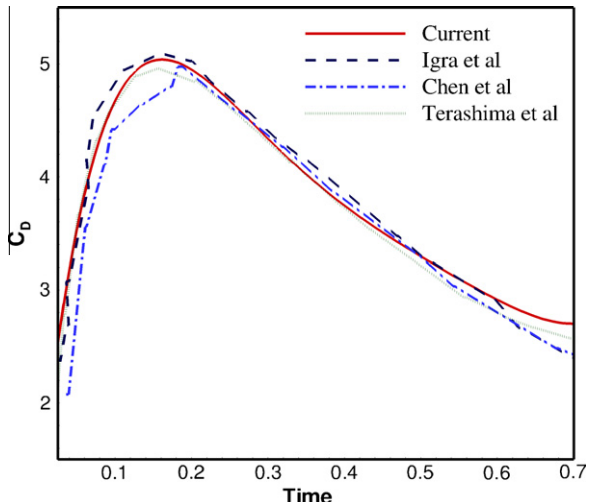


**Fig. 19.** Comparison of unsteady drag coefficient computed on the surface of a cylindrical droplet.

waves interacting with *cylindrical* water column(s) have been investigated and well documented in the past [47,14,15,31]. Here the interaction of planar shock waves with a *spherical* water droplet suspended in ambient air is investigated. Two different shock strengths, Mach 1.47 and 6.0, are considered. The spherical liquid mass of radius 0.105 mm is located at (0.0, 0.5) in a  $0.5 \text{ mm} \times 1.0 \text{ mm}$  domain. Euler equations in the axisymmetric form are solved for this problem. The simulations are carried out on a base mesh of size  $\Delta x_g = \frac{1}{200}$  with 3–5 (corresponding to 5.12 million grid points when the mesh is distributed uniformly throughout the domain) levels of mesh refinement.

The shock systems observed for the interaction of planar shock wave with spherical and cylindrical droplets are identical, except for the strengths of the reflected and refracted shock systems. The configuration forms a curved gas–liquid slow–fast interface [47]. As pointed out in [15], the shock wave upon impacting the water column transmits only a small fraction of the energy into the water medium due to large acoustic impedance. As a result of this impedance mismatch, a reflected and a refracted shock systems are generated. The refracted weak shock wave on the water side travels faster than the incident shock wave and is reflected

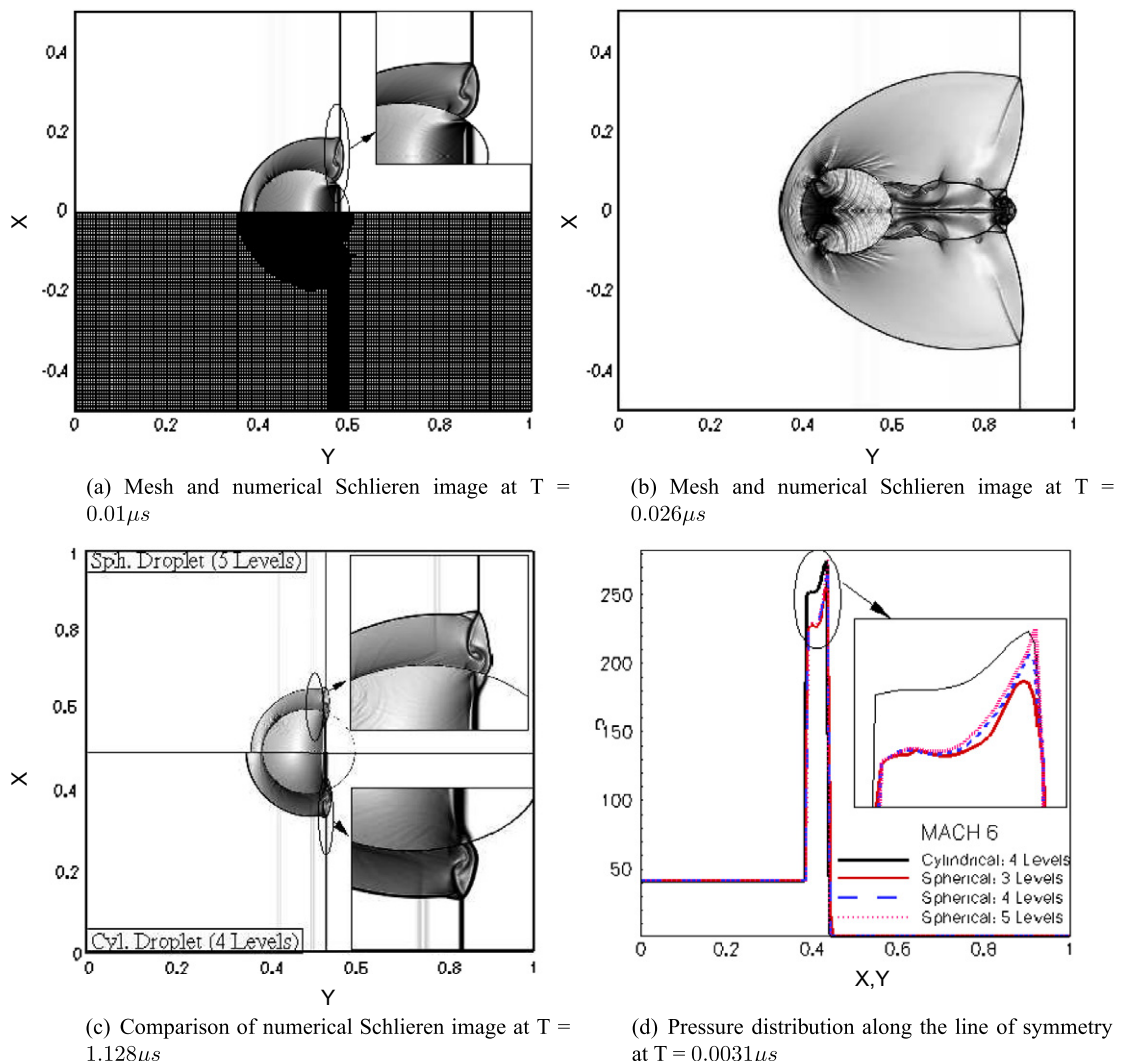


**Fig. 20.** Mach six shock interacting with spherical water droplet: (a) and (b) Snapshots of mesh evolution and numerical Schlieren image at  $T = 0.01 \mu\text{s}$  and at  $T = 0.026 \mu\text{s}$ , respectively, computed on a base mesh  $\Delta x_g = \frac{1}{200}$  with 4 levels of refinement; (c) Comparison with cylindrical droplet computed on a base mesh  $\Delta x_g = \frac{1}{200}$  with four levels of refinement; (d) Pressure distribution along the line of symmetry at  $T = 0.0031 \mu\text{s}$ .

back as a “relief wave” by the curved interface. As pointed out by Chang et al. [14], due to the curvature of the interface these rarefaction waves later coalesce to form a shock wave. Thus the refracted shock wave gets trapped inside the water column by undergoing multiple reflections off the curved interface and hence does not affect the surrounding air. In what follows, the shock diffraction patterns generated for different shock strengths are briefly examined.

**5.2.4.1. Effect of mach 1.47 shock interacting with spherical water droplet.** The threshold for the refinement criteria were set at  $\delta_1 = 1.0$  and  $\delta_2 = 75.0$ . The results from the current calculations with five levels of mesh refinement are displayed in Fig. 18. The reflected, refracted and the incident shock systems along with the “peeling off” effect on the bubble (reported in [47]) are clearly visible. In Fig. 18d, the pressure distribution along the axis of symmetry are plotted for both the cylindrical and the spherical bubble. In comparison with the cylindrical water column, the strengths (pressure ratio) of the reflected and the transmitted shock waves are significantly lower for the spherical droplet (three-dimensional effect). Fig. 18d also confirms the mesh independence of the solution. The OR for this calculation is 10.0%.

For validating the current approach, a comparison of the unsteady drag coefficient computed on the surface of a *cylindrical* droplet is presented in Fig. 19. The drag coefficient is compared with that of Igra et al. [31], Chen [15] and Terashima et al. [69]. The drag coefficient distribution predicted with the current method is in good agreement with available solutions.

**5.2.4.2. Effect of mach 6 shock interacting with spherical water droplet.** The threshold for the refinement criteria were set at  $\delta_1 = 10.0$  and  $\delta_2 = 150.0$ . The shock diffraction patterns for this case are displayed in Fig. 20. A double Mach reflection system, as opposed to a single Mach system, is formed. The double Mach stem is not visible in Fig. 20a, but is visible in Fig. 20c with additional mesh resolution (with  $\Delta x_f = \frac{1}{3200}$ ). The pressure distribution along the line of symmetry displayed in Fig. 20d confirms convergence of solution with mesh refinement. The increase in refinement level only accentuates fine structures that are otherwise not visible. The strengths of the reflected and refracted shock systems are comparable. The OR for this calculation is 13.3%.

### 5.2.5. Diffraction patterns generated by supersonic bluff-body projectile

Previous investigations [34,33,56] on ballistics of projectiles were limited to stationary or moving projectiles with simple square or rectangular shapes that conform to the computational mesh. The experimental and the numerical simulations documented for this problem were focused on the initial unsteady shock wave diffraction phenomena (such as the blast wave, the jet flow, the vortex ring, etc.) generated due to the movement of the projectile in the vicinity of the outlet of the launch tube. In this example, a realistic scenario of a bluff body projectile fired at Mach 1.22 moving through the mesh (as opposed to solving in a moving coordinate system attached to the projectile) is studied. Attention

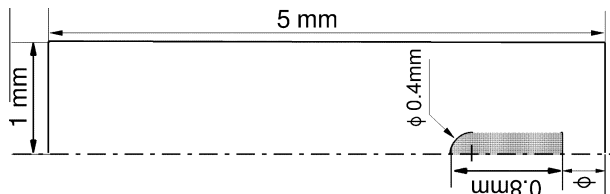


Fig. 21. Configuration of a projectile travelling at Mach 1.22.

is paid to the later part of the projectile motion and the resultant diffraction patterns. Configuration of the system and the computational domain are displayed in the Fig. 21. The simulation was carried out with base mesh of size  $\Delta x_g = 0.02$  with five levels of mesh refinement (an effective resolution of 3.2 million grid points when distributed uniformly throughout the computational domain). The threshold for the refinement criteria were set at  $\delta_1 = 1.0$  and  $\delta_2 = 1.0$ .

The numerical Schlieren image along with the mesh topology generated from the current simulations are displayed in Fig. 22. The initial movement of the projectile results in a series of compression waves that coalesce to form the “bow shock” that stands

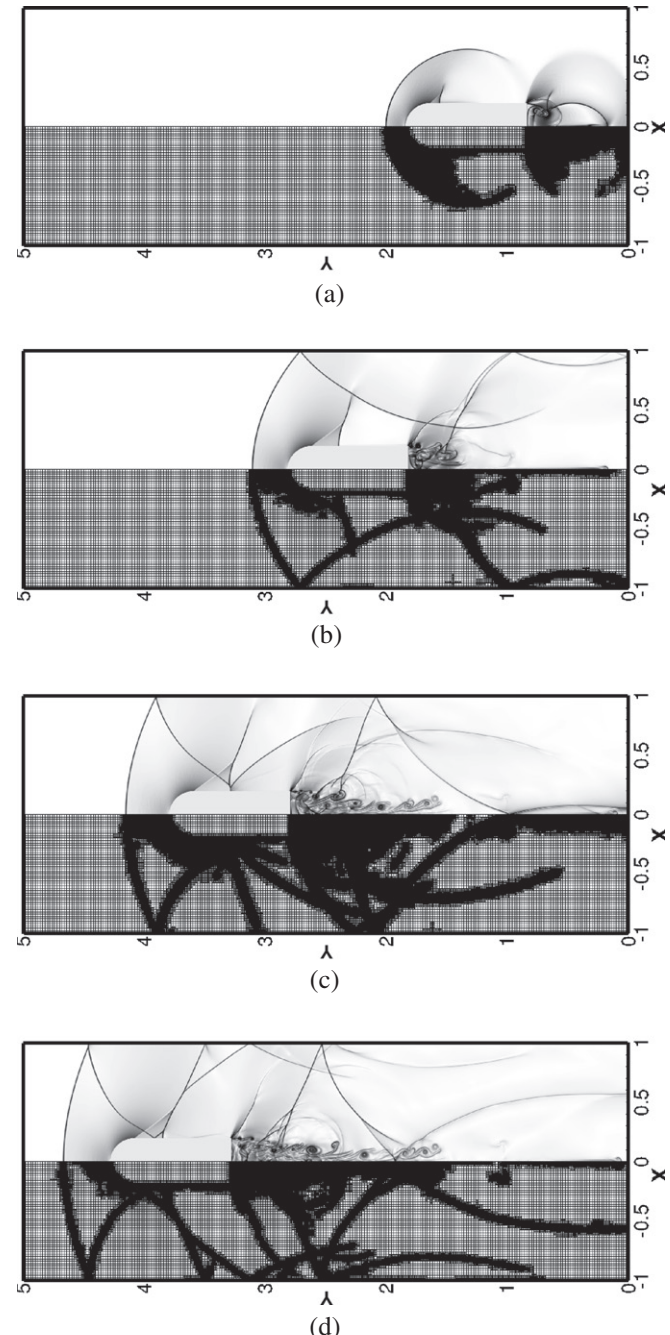
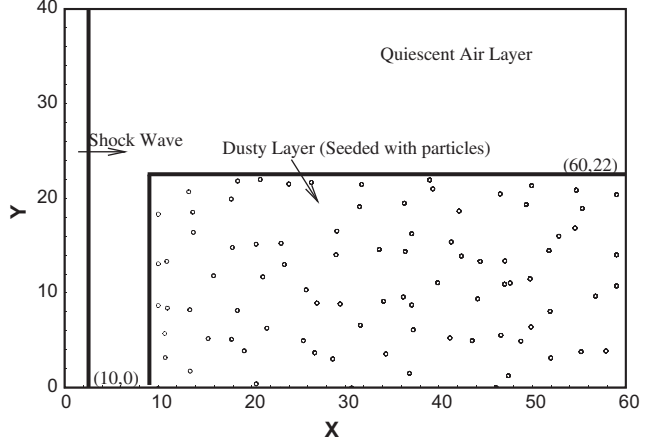


Fig. 22. Numerical Schlieren image and the mesh topology at different instants in time, for a supersonic projectile fired at Mach 1.22, computed on a base mesh of size  $\Delta x_g = 0.1$  with five levels of mesh refinement: (a)  $T = 0.25$  ms; (b)  $T = 0.565$  ms; (c)  $T = 4.65$  ms; (d)  $T = 7.03$  ms.

off from the nose of the projectile (Fig. 22a). The diffraction pattern observed at the rear end of the projectile is similar to that of shock wave negotiating 90° step. Fig. 22a shows the Prandtl-Meyer expansion waves and slip-lines generated at the rear end of the projectile. As expected, the slip-lines eventually roll up to form vortices (vortex rings in this case). These vortices are clearly visible in Fig. 22b. Fig. 22c and d correspond to the instant at which the projectile has moved sufficiently far away from the launch tube/pad. At the front end of the projectile, the bow shock formed stands off sufficiently far away from the nose of the projectile. At the rear end of the projectile, the barotropic vortices generated are convected downstream relative to the movement of the projectile (Fig. 23a). In Fig. 23b the front end bow shock stand-off distance is plotted as a function of time. The shock stand-off distance increases linearly with time, for time  $T \leq 0.5$  ms, and subsequently reaches a steady state value of 0.22 units (0.55 body diameter) which is typical of projectile fired at transonic Mach numbers [32]. Fig. 22a-d indicate that evolution of the mesh closely follows the primary features in the flow field. The occupancy ratio computed for this simulation is 23.25%.

#### 5.2.6. Shock diffraction patterns in a dusty cloud

In this example, the DNS of a planar shock wave traversing through a dusty gas layer is performed. In [22], the problem was investigated by solving the Euler equations using a mixture model. Here the corresponding DNS calculations for two different



**Fig. 24.** Initial configuration of the system for DNS of shock wave traversing through a dusty layer of gas.

Mach numbers (1.67 and 3) are performed. The initial configuration of the system is shown in Fig. 24. A layer of (100) particles, with density  $\rho = 1000$ , are randomly seeded (Fig. 24) in a computational domain of size 60 mm × 40 mm. The radius of the particles ( $d = 0.2$  mm) and the mass fraction ( $M = 0.005$ ) chosen for the

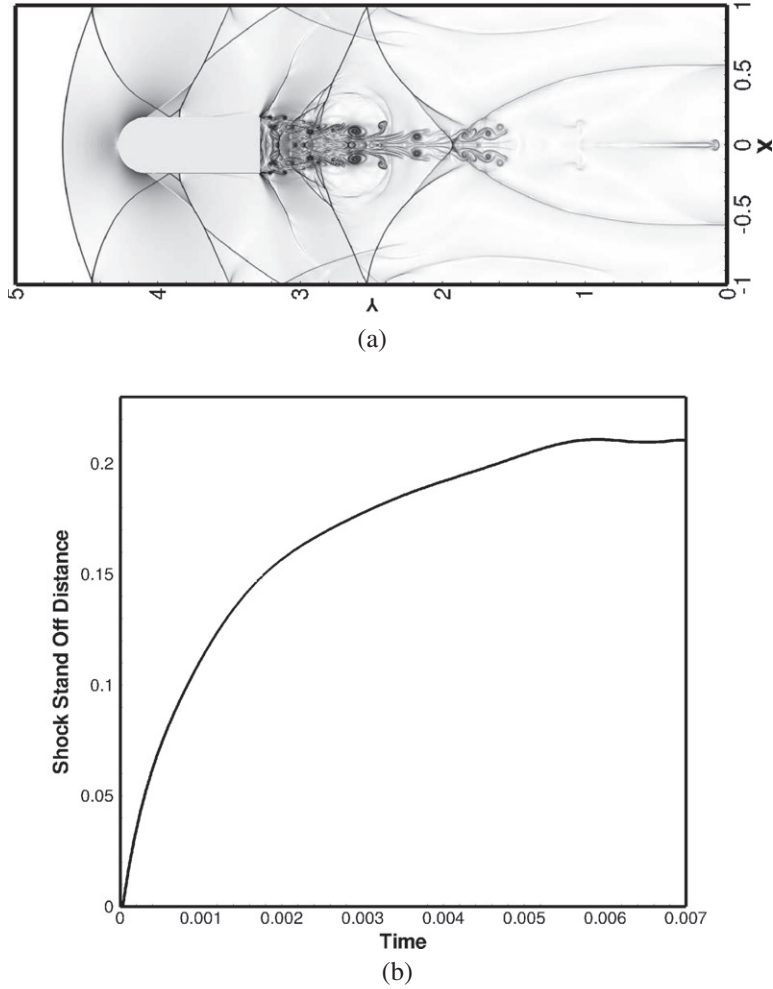


**Fig. 23.** (a) Numerical Schlieren image at time  $T = 7.03$  ms; (b) Shock stand off as a function of time, for the bluff body projectile fired at Mach 1.22.

current calculations are slightly higher than in [22]. The present computations are performed on a base mesh of size  $\Delta x_g = 0.25d$  with four levels of mesh refinement (13 points per diameter) resulting in an effective resolution of about 2.45 million grid points. The threshold for the refinement criteria were set at  $\delta = 1.0$  and  $\delta = 25.0$ . Fig. 25 shows the complex shock diffraction patterns generated for a shock of Mach 1.67 interacting with the dust particles. The inserts in the figure display the enlarged view of the shock patterns in the wake region and the mesh adhering to these complex patterns. In Fig. 26 the contours of barotropic vortices are plotted for the same Mach number. Inserts in the figure show the intricate vortical patterns observed in the wake region and the mesh topology conforming to these vortices. Thus from Fig. 25, it is clear that the mesh adaptation strategies

developed in this work are effective in identifying and resolving regions with active structures and steep gradients. Next the Mach number is increased to 3.0 and the calculation is repeated. The numerical Schlieren image depicting the shock patterns for the high Mach number case is displayed in Fig. 27. The method is found to be stable even for high Mach numbers. The wake patterns shown in Figs. 25–27 were not reported in the previous mixture model-based calculations [22]. Furthermore, the effect of viscosity on the wake patterns is an open subject of investigation. It is believed that the current effort is a step towards DNS of such large scale computations. Presently, efforts are underway for large scale computations (with large number of particles ( $O(1000)$ ) with smaller radius ( $O(1 \mu\text{m})$ )) and the results will be reported in a separate work.

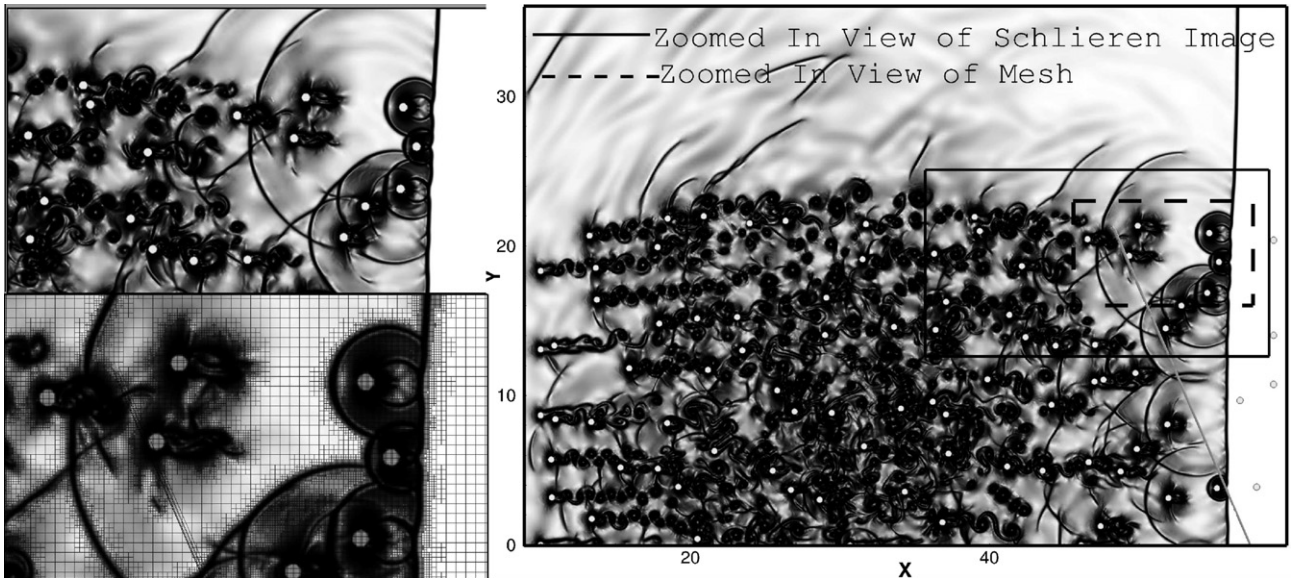


**Fig. 25.** Numerical Schlieren image for a Mach 1.67 shock wave traversing through a dusty layer of gas at time  $T = 76.15 \mu\text{s}$ .

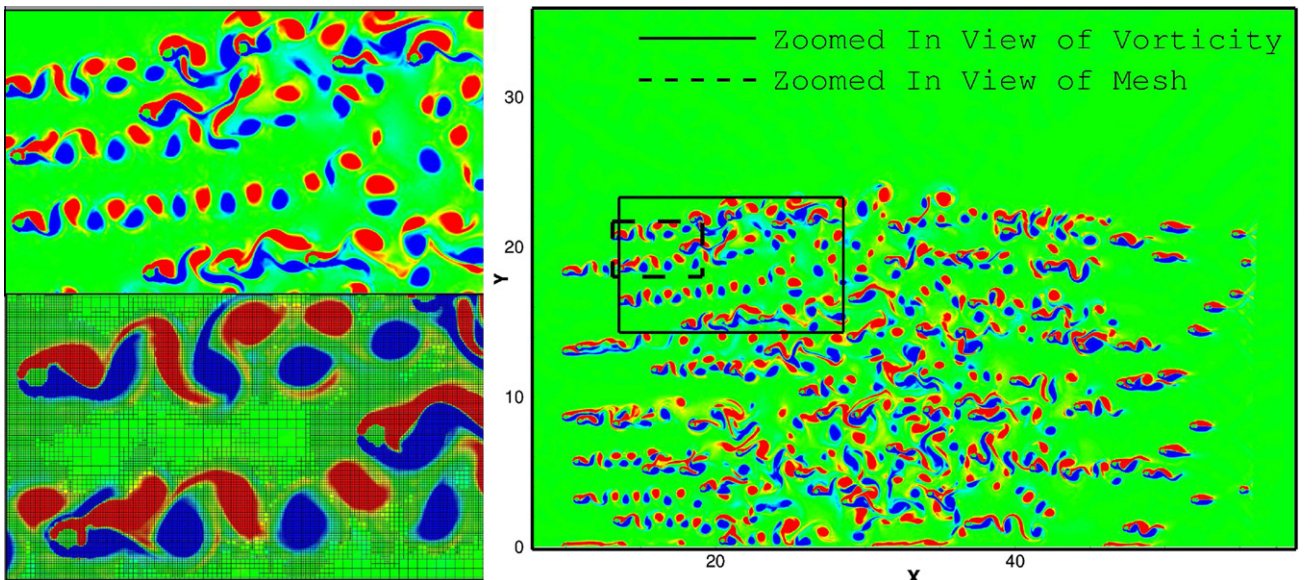


**Fig. 26.** Vorticity contours for a Mach 1.67 shock wave traversing through a dusty layer of gas at time  $T = 76.15 \mu\text{s}$ .

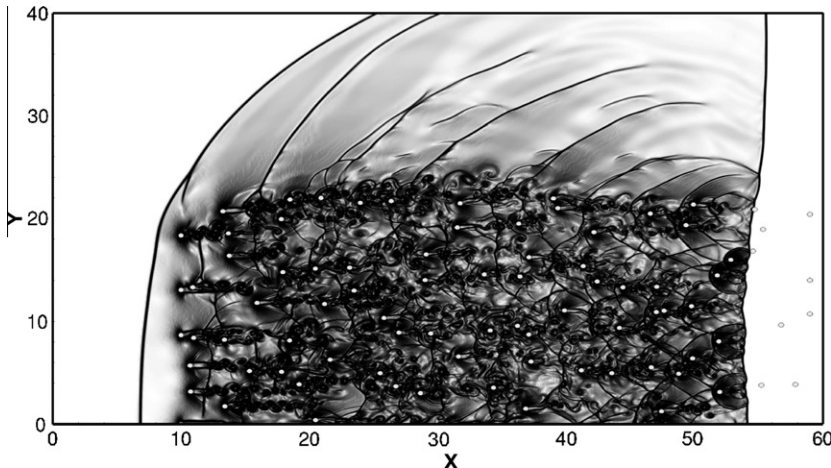


**Fig. 27.** Numerical Schlieren image for a Mach 3 shock wave traversing through a dusty layer of gas at time  $T = 41.17 \mu\text{s}$ .

## 6. Conclusions

The paper reports on a simple and efficient approach for coupling tree-based Local Mesh Refinement (LMR) schemes with higher-order numerical schemes such as ENO for high fidelity and highly efficient computations of high speed compressible multiphase flows. The embedded objects were retained as sharp entities by virtue of the unified Riemann solver based Ghost Fluid Method (GFM) developed in [55,54]. Quadtree-based (octree in three dimensions) Local Mesh Refinement (LMR) scheme developed [38] was used to resolve dominant structures and steep gradients in the flowfield. A conservative, bilinear interpolation scheme was formulated to construct numerical fluxes at the fine-coarse mesh boundary. The method provides a simple framework to uniformly integrate ENO schemes by retaining the simplicity associated with the uniform mesh based flux re-construction approach. The numerical examples clearly demonstrates that the methodology developed in this work is consistent in generating satisfactory solutions without sacrificing the speed and accuracy of the solution. Furthermore, the occupancy ratio (OR) reported in this work shows the effectiveness of the scheme in economically resolving the desired physics.

## Acknowledgements

The work was performed under the grants from the AFOSR computational mathematics group (Program Manager: Dr. Fariba Fahroo) and from the AFRL-MNAC (Eglin AFB, Program Manager: Dr. Michael E. Nixon).

## References

- [1] Abgrall R. On essentially non-oscillatory schemes on unstructured meshes: analysis and implementation. *J Comput Phys* 1994;114(1):45–58.
- [2] Agresar G, Linderman JJ, Tryggvason G, Powell KG. An adaptive, cartesian, front-tracking method for the motion, deformation and adhesion of circulating cells. *J Comput Phys* 1998;143(2):346–80.
- [3] Andreea Sigrid, Ballmann Josef, Müller Siegfried. Analysis and numerics for conservation laws, chapter wave processes at interfaces. Berlin Heidelberg: Springer; 2005.
- [4] Banks JW, Schwendeman DW, Kapila AK, Henshaw WD. A high-resolution godunov method for compressible multi-material flow on overlapping grids. *J Comput Phys* 2007;223(1):262–97.
- [5] Bazhenova TV, Gvozdeva LG, Nettleton MA. Unsteady interactions of shock waves. *Prog Aerospace Sci* 1984;21:249–331.
- [6] Benson David J. Computational methods in lagrangian and eulerian hydrocodes. *Comput Methods Appl Mech Eng* 1992;99(2–3):235–394.
- [7] Berger MJ, Colella P. Local adaptive mesh refinement for shock hydrodynamics. *J Comput Phys* 1989;82(1):64–84.
- [8] Marsha J. Berger, Joseph E. Oliger. Adaptive mesh refinement for hyperbolic partial differential equations. Technical report, Stanford (CA, USA); 1983.
- [9] Braun Jean, Sambridge Malcolm. A numerical method for solving partial differential equations on highly irregular evolving grids. *Nature* 1995;376:655–60.
- [10] Browning Gerald, Kreiss Heinz-Otto, Oliger Joseph. Mesh refinement. *Math Comput* 1973;27(121):29–39.
- [11] Bryson AE, Gross RWF. Diffraction of strong shocks by cones, cylinders and spheres. *J Fluid Mech* 1960;10:1–16.
- [12] Casper Jay, Atkins HL. A finite-volume high-order eno scheme for two-dimensional hyperbolic systems. *J Comput Phys* 1993;106(1):62–76.
- [13] Cecil Thomas C, Osher Stanley J, Qian Jianliang. Essentially non-oscillatory adaptive tree methods. *J Sci Comput* 2008;35(1):25–41.
- [14] Chang CH, Liou MS. A robust and accurate approach to computing compressible multiphase flow: stratified flow model and AUSM+ – up scheme. *J Comput Phys* 2007;225:840–73.
- [15] Chen H, Liang SM. Flow visualization of shock/water interactions. *Shock Waves* 2008;17:309–21.
- [16] Choi Dae-II, David Brown J, Imbiriba Breno, Centrella Joan, MacNeice Peter. Interface conditions for wave propagation through mesh refinement boundaries. *J Comput Phys* 2004;193(2):398–425.
- [17] Cocco JP, Saurel R, Loraud1 JC. Treatment of interface problems with Godunov-type schemes. *Shock Waves* 1996;5(6):347–57.
- [18] Coirier William J, Powell Kenneth G. An accuracy assessment of Cartesian-mesh approaches for the euler equations. *J Comput Phys* 1995;117(1):121–31.
- [19] William John Coirier. An adaptively-refined, Cartesian, cell based scheme for the Euler and Navier-Stokes equations. PhD thesis. Ann Arbor (MI, USA); 1994.
- [20] de Tullio MD, De Palma P, Iaccarino G, Pascazio G, Napolitano M. An immersed boundary method for compressible flows using local grid refinement. *J Comput Phys* 2007;225(2):2098–117.
- [21] Drakakis D, Ofengheim D, Timofeev E, Voionovich P. Computation of non-stationary shock-wave/cylinder interaction using adaptive grid methods. *J Fluid Struct* 1997;11:665–91.
- [22] Federov AV, Kharlamova Yu V, Khmel TA. Reflection of a shock wave in a dust cloud. *Combust Explos Shock Waves* 2007;43(1):104–13.
- [23] Fedkiw RP, Aslam TD, Merriman B, Osher S. A non oscillatory Eulerian approach to interfaces in multi-material flows (the ghost fluid method). *J Comput Phys* 1999;152(2):457–92.
- [24] Greaves DM, Borthwick AGL. On the use of adaptive hierarchical meshes for numerical simulation of separated flows. *Int J Numer Methods Fluids* 1998;26(3):303–22.
- [25] Greaves DM, Borthwick AGL. Hierarchical tree-based finite element mesh generation. *Int J Numer Methods Fluids* 1999;45(4):447–71.
- [26] Greaves Deborah M. Hierarchical tree-based finite element mesh generation. *Int J Numer Methods Fluids* 2004;44(10):1093–117.
- [27] Greaves Deborah M. A quadtree adaptive method for simulating fluid flows with moving interfaces. *J Comput Phys* 2004;194(1):35–56.
- [28] Griffith Boyce E, Hornung Richard D, McQueen David M, Peskin Charles S. An adaptive, formally second order accurate version of the immersed boundary method. *J Comput Phys* 2007;223(1):10–49.
- [29] Harlow F, Amsden A. Fluid dynamics. Technical report, Los Alamos National Laboratory Monograph; 1971.
- [30] Henshaw WD, Schwendeman DW. Moving overlapping grids with adaptive mesh refinement for high-speed reactive and non-reactive flow. *J Comput Phys* 2006;216(2):744–79.
- [31] Igra D, Takayama K. Numerical simulation of shock wave interaction with water column. *Shock Waves* 2001;11:219–28.
- [32] Glass II. Shock waves and man. The University of Toronto Press; 1974.

- [33] Jian Xiaohai, Chen Zhihua, Fan Baochun, Li Hongzhi. Numerical simulation of blast flow fields induced by a high-speed projectile. *Shock Waves* 2008;18:205–12.
- [34] Jiang Zonglin, Huang Yonghui, Takayama Kazuyoshi. Shocked flows induced by supersonic projectiles moving in tubes. *Comput Fluids* 2004;33(7):953–66.
- [35] Kaca J. An interferometric investigation of the diffraction of a planar shock wave over a semicircular cylinder. Technical report 269, University of Toronto, Institute for Aerospace Studies (UTIAS); 1988.
- [36] Karni Smadar, Kurganov Alexander, Petrova Guergana. A smoothness indicator for adaptive algorithms for hyperbolic systems. *J Comput Phys* 2002;178(2):323–41.
- [37] Keppens R, Nool M, Tóth G, Goedbloed JP. Adaptive mesh refinement for conservative systems: multi-dimensional efficiency evaluation. *Comput Phys Commun* 2003;153(3):317–39.
- [38] Krishnan S. An adaptively refined Cartesian grid method for moving boundary problems applied to biomedical systems. PhD thesis, The University of Iowa; 2006.
- [39] Kurganov Alexander, Tadmor Eitan. Solution of two-dimensional Riemann problems for gas dynamics without Riemann problem solvers. *Numer Methods Partial Differ Equat* 2002;18:584–608.
- [40] Liu TG, Khoo BC, Yeo KS. Ghost fluid method for strong shock impacting on material interface. *J Comput Phys* 2003;190:651–81.
- [41] Liu XD, Osher S. Convex ENO high order multi-dimensional schemes without field by field decomposition or staggered grids. *J Comput Phys* 1998;142:304–30.
- [42] Losasso Frank, Fedkiw Ronald, Osher Stanley. Spatially adaptive techniques for level set methods and incompressible flow. *Comput Fluids* 2005;35:2006.
- [43] Frank Losasso, Frédéric Gibou, Ron Fedkiw. Simulating water and smoke with an octree data structure. In: SIGGRAPH '04: ACM SIGGRAPH 2004 papers. New York (NY, USA): ACM; 2004. p. 457–62.
- [44] Marquina A, Mulet P. A flux-split algorithm applied to conservative models for multicomponent compressible flows. *J Comput Phys* 2003;185:120–38.
- [45] Menikoff Ralph, Plohr Bradley J. The Riemann problem for fluid flow of real materials. *Rev Mod Phys* 1989;61(1):75.
- [46] Min Chohong, Gibou Frédéric. A second order accurate level set method on non-graded adaptive cartesian grids. *J Comput Phys* 2007;225(1):300–21.
- [47] Nourgaliev RR, Dinh TN, Theofanous TG. Adaptive characteristics-based matching for compressible multi-fluid dynamics. *J Comput Phys* 2006;213:500–29.
- [48] Osher S, Sethian JA. Fronts propagating with curvature dependent speed algorithms based on Hamilton–Jacobi. *J Comput Phys* 1988;79:12–49.
- [49] Popinet Stéphane. Gerris: a tree-based adaptive solver for the incompressible Euler equations in complex geometries. *J Comput Phys* 2003;190(2):572–600.
- [50] Quirk James J. A parallel adaptive grid algorithm for computational shock hydrodynamics. *Appl Numer Math* 1996;20(4):427–53.
- [51] Quirk JJ. An adaptive grid algorithm for computational shock hydrodynamics. PhD thesis, Cranfield Institute of Technology; 1991.
- [52] Quirk JJ, Karni S. On the dynamics of shock bubble interaction. *J Fluid Mech* 1996;318:129–63.
- [53] Ripley RC, Lien FS, Yovanovich MM. Numerical simulation of shock diffraction on unstructured meshes. *Comput Fluids* 2006;35:1420–31.
- [54] Sambasivan S, UdayKumar HS. Evaluation of ghost-fluid methods for strong shock interactions. Part II: immersed solid boundaries. *AIAA J* 2009;47(12):2923–37.
- [55] Sambasivan S, UdayKumar HS. Evaluation of ghost fluid methods for strong shock interactions. Part I: fluid–fluid interfaces. *AIAA J* 2009;47(12):2907–22.
- [56] Saurel R, Cocchi P, Butler PB. Numerical study of cavitation in the wake of a hypervelocity underwater projectile. *J Propul Power* 1999;15:513–22.
- [57] Scott Stewart D, Yoo SL. High resolution numerical simulation of ideal and non-ideal compressible reacting flows with embedded internal boundaries. *Combus Theory Model* 1997;1:113–42.
- [58] Sebastian Kurt, Shu Chi-Wang. Multidomain weno finite difference method with interpolation at subdomain interfaces. *J Sci Comput* 2003;19(1–3):405–38.
- [59] Shu CW, Osher S. Efficient implementation of essentially non-oscillatory shock capturing schemes II. *J Comput Phys* 1989;83:32–78.
- [60] Sochinski Vassili, Efrima Shlomo. Level set calculations of the evolution of boundaries on a dynamically adaptive grid. *Int J Numer Methods Eng* 2003;56(13):1913–29.
- [61] Strain John. Fast tree-based redistancing for level set computations. *J Comput Phys* 1999;152(2):664–86.
- [62] Strain John. Semi-Lagrangian methods for level set equations. *J Comput Phys* 1999;151(2):498–533.
- [63] Strain John. Tree methods for moving interfaces. *J Comput Phys* 1999;151(2):616–48.
- [64] Strain John. A fast modular semi-Lagrangian method for moving interfaces. *J Comput Phys* 2000;161(2):512–36.
- [65] Sukumar N, Moran Brian, Belytschko Ted B. The natural element method in solid mechanics. *Int J Numer Methods Eng* 1998;43(5):839.
- [66] Mingyu Sun. Numerical and Experimental Investigation of Shock Wave Interactions with Bodies. PhD thesis, Tohoku University, 1998.
- [67] Sussman Mark, Fatemi Emad. An efficient interface-preserving level set redistancing algorithm and its application to interfacial incompressible fluid flow. *SIAM J Sci Comput* 1999;20(4):1165–91.
- [68] Takayama K, Itoh K. Unsteady drag over cylinders and aerofoils in transonic shock tube ows. In: Bershadier D, Hanson R, editors. Proceedings of the 15th international symposium on shock waves and shock tubes. Berkeley, California: Stanford University Press; July 28–August 2, 1985.
- [69] Terashima Hiroshi, Tryggvason Grtar. A front-tracking/ghost-gluid method for fluid interfaces in compressible flows. *J Comput Phys* 2009;228(11):4012–37.
- [70] Toro EF. Riemann solvers and numerical method for fluid dynamics – a practical introduction. 2nd ed. Springer; 1997.
- [71] Tran LB, UdayKumar HS. A particle levelset based sharp interface Cartesian grid method for impact, penetration, and void collapse. *J Comput Phys* 2004;193:469–510.
- [72] UdayKumar HS, Krishnan S, Marella S. refined Adaptively. parallelised sharp interface cartesian grid method for three-dimensional moving boundary problems. *Int J Comput Fluid Dynam* 2009;23:1061–8562.
- [73] UdayKumar HS, Tran L, Belk DM, Vandem KL. An Eulerian method for computation of multi-material impact with ENO shock-capturing and sharp interfaces. *J Comput Phys* 2003;186:136–77.
- [74] Wang C, Tang H, Liu TG. An adaptive ghost fluid finite volume method for compressible gas–water simulations. *J Comput Phys* 2008;227(12):6385–409.
- [75] Wang ZJ. A quadtree-based adaptive Cartesian/quad grid flow solver for Navier–Stokes equations. *Comput Fluids* 1998;27(4):529–49.
- [76] Xu S, Aslam TD, Scott Stewart D. High resolution numerical simulation of ideal and non-ideal compressible reacting flows with embedded internal boundaries. *Combus Theory Model* 1997;1:113–42.
- [77] Darren L. De Zeeuw. A quadtree-based adaptively-refined Cartesian-grid algorithm for solution of the Euler equations. PhD thesis, Ann Arbor (MI, USA); 1993.
- [78] Ziegler Udo. A three-dimensional cartesian adaptive mesh code for compressible magnetohydrodynamics. *Comput Phys Commun* 1999;116(1):65–77.